RSC Advances

RSC Publishing

REVIEW

View Article Online
View Journal | View Issue

Electrode materials for aqueous asymmetric supercapacitors

Cite this: *RSC Advances*, 2013, **3**, 13059

Faxing Wang, Shiying Xiao, Yuyang Hou, Chenglin Hu, Lili Liu and Yuping Wu*

Received 25th December 2012,
Accepted 16th April 2013

DOI: 10.1039/c3ra23466e

www.rsc.org/advances

An asymmetric supercapacitor (ASC) is a supercapacitor based on two different electrode materials. One electrode is based on redox (Faradic) reactions with or without non-faradic reactions, and the other one is mostly based on electric double-layer (non-Faradic or electrostatic) absorption/desportion. Aqueous electrolytes have higher ionic conductivity, larger capacitance and better safety than the organic electrolytes. Herein, some key electrode materials for aqueous ASCs are primarily reviewed, which provide a new direction for power sources to have higher energy density at high power densities, compared with traditional capacitors. Their negative electrode materials include carbonaceous materials (porous carbons, carbon nanotubes and graphene), oxides (V_2O_5 and MoO_3) and their composites, and their positive electrode materials include carbonaceous materials, oxides (RuO_2, MnO_2, MoO_3, V_2O_5, PbO_2, Co_3O_4), $Ni(OH)_2$, intercalation compounds ($LiCoO_2$, $LiMn_2O_4$, $Li[NiCoMn]_{1/3}O_2$, $NaMnO_2$ and $KMnO_2$). We describe the latest work on these electrode materials, and a particular focus is directed to the fabrication and electrochemical performance of various nanostructured electrode materials and some assembled ASCs. Finally, the future trends and prospects on advanced energy storage materials are suggested.

Published on 16 avril 2013. Downloaded on 2024-08-15 14:15:36.

1. Introduction

Recently, there has been an increasing demand for environmentally friendly and high-performance supercapacitors, which have found important applications in rapidly expanding markets, especially in electric vehicles (EVs) and smart grids. The EV is a promising ''zero-emission'' vehicle, which is expected to significantly contribute to solving the problems of global warming and environmental pollution. Supercapacitors can be coupled with batteries and fuel cells to provide peak power in all-electric vehicles and replace batteries for memory back-up, which makes them probably one of the most important energy storage devices. Smart grids are also very important to increase the power efficiency and utilize renewable energies.[1]

Currently, supercapacitors have several types, which are briefly listed in Table 1, and they can store hundreds or thousands of times more charge than the conventional capacitors. However, their energy density is still lower compared with batteries and fuel cells. Therefore, one of the most critical aspects in the development of hybrid supercapacitors (HSCs) is to enhance their energy density while retaining their intrinsic high specific power. Many different systems including different materials have been investigated extensively; however, so far there is no unambiguous definition of HSC. These kinds of HSC systems were firstly named ''asymmetric supercapacitors''.[2a,2b] The term ''hybrid capacitor'' was first introduced and trademarked by Evans Capacitor Company.[2c] Here, hybrid supercapacitors (HSCs) include composite symmetric supercapacitors, battery–supercapacitor hybrids and asymmetric supercapacitors (ASCs). ASCs usually consist of two different electrodes. During charge and discharge processes, one electrode should take place redox (Faradic) reactions with or without non-faradic reactions, and

New Energy and Materials Laboratory (NEML), Department of Chemistry & Shanghai Key Laboratory of Molecular Catalysis and Innovative Materials, Fudan University, Shanghai 200433, China. E-mail: wuyp@fudan.edu.cn; Fax: +86-21-5566 4223; Tel: +86-21-5566 4223

Yuping Wu

Dr Yuping Wu is a professor at Fudan University, Shanghai, China. Since 1994, he has published over 190 peer-reviewed papers, written five monographs whose sales are above 23000 copies and 4 chapters, translated one book, got 19 issued patents. H-index is 32. His research has led to the creation of three companies on anode materials, cathode materials and power lithium ion batteries, respectively. His research is mainly focused on lithium ion batteries, supercapacitors, other new energy storage and conversion systems and solar hydrogen.

This journal is © The Royal Society of Chemistry 2013

Published on 16 avril 2013. Downloaded on 2024-08-15 14:15:36.

Table 1 Some characteristics of several types of supercapacitors

Types		Mechanisms	Materials	Merits	Shortcomings
EDLCs		Charge separation at the electrode–electrolyte interface	Carbon materials	High power density, and good cycling behaviors	Low energy density, and low working voltage
Pseudo-capacitors		Reversible surface Faradic redox reactions	Transition metal oxides, conducting polymers	High capacitance and energy density	Poor cycling behavior, and low working voltage
	Composite symmetric	Two electrodes are the same and present electric double-layer absorption/desorption and Faradic redox reactions.	Composites of pseudo-capacitive materials with carbon materials	Relatively high energy and power densities	Low working voltage
HSCs	ASCs	Redox reaction(s) for one electrode and electric double-layer absorption/desorption for the other electrode	Porous carbons, graphene, oxides, conductive polymers, lithium intercalation compounds	Relatively high energy and power densities, and good cycling	Almost every performance is at the intermediate level
	Battery-typed	Redox reactions for both electrodes.	Lithium intercalation compounds	High energy density and working voltage	Poor cycling behaviors, low power density

the other one mostly taking place is electric double-layer (EDL) (non-Faradic or electrostatic) absorption/desportion.[2d] The structure of ASCs can be schematically illustrated in Fig. 1.

In terms of ASCs, there are two important parameters: energy density (E) and power density (P). The expressions of both parameters are shown as eqn (1) and (2).[3]

$$E = \frac{1}{2}CV^2 \quad (1)$$

$$P = \frac{V^2}{4R} \quad (2)$$

Where V is working voltage, C the specific capacitance of the electrode materials and R the internal resistance.

In order to achieve large E and P, both C and V are needed to increase. The working voltage, V, is mainly limited by electrolytes, and thus ASCs are mainly classified into two types based on electrolytes: aqueous and nonaqueous.[4a,4b] At present, most commercial products use organic electrolytes, which offer a wider electrochemical window. Although the working voltage of organic electrolytes can be up to 3V,[4c] they are associated with safety risks because of the flammability of the organic electrolytes and improper use such as over-charging or short-circuiting. Their practical energy density is not high, and most of them are below 5 Wh kg^{-1}. The main reason is that C is not large enough due to the large sizes of the organic molecules. In fact, aqueous electrolytes have significant inherent advantages over organic electrolytes:

• The cost of the aqueous electrolyte is low because the expensive salts can be replaced by cheap ones.

• The assembling process is easy, and high-cost devices and assembly techniques are not required.

• It is inherently safe by avoiding the use of flammable organic electrolytes.

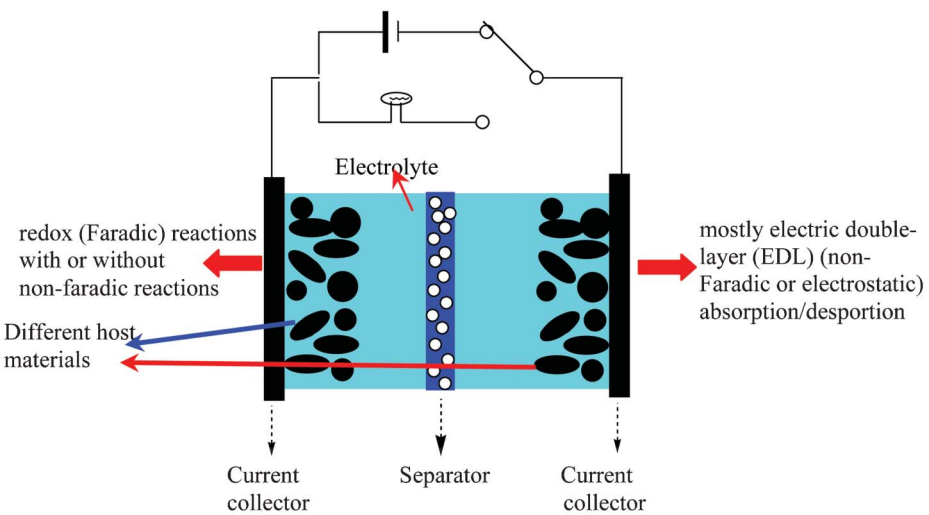

Fig. 1 Schematic illustration of ASCs.

 This journal is © The Royal Society of Chemistry 2013

Published on 16 avril 2013. Downloaded on 2024-08-15 14:15:36.

Table 2 Some aqueous ASCs and their primary characteristics

Negative materials	Positive materials	Electrolytes	Working voltage	Rate behavior	Cycling performance[a]	Ref.
AC	V_2O_5	0.5 mol l^{-1} K_2SO_4	0–1.8 V	—	100	6*a*
PPy@V_2O_5	AC	0.5 mol l^{-1} K_2SO_4	0–1.8 V	—	10 000(>95%)	6*b*
MoO_3 nanoplates	AC	0.5 mol l^{-1} Li_2SO_4	0–1.8 V	2 A g^{-1}	400	6*c*
AC	RuO_2@TiO_2 nanotube	1 mol l^{-1} KOH	0–1.4 V	0.12 A cm^{-2}	1000(>90%)	6*d*
AC	MnO_2	0.1 mol l^{-1} K_2SO_4 (without O_2)	0–2 V	40 mA cm^{-2}	195 000	7*a*
AC	MnO_2@AC	0.5 mol l^{-1} Na_2SO_4	0–1.8 V	12.74 mA cm^{-2}	1500	7*b*
AC	MnO_2 nanorod	0.5 mol l^{-1} K_2SO_4	0–1.8 V	10 C	23 000 (100%)	7*c*
AC	Nanowires MnO_2 @MWCNTs	0.5 mol l^{-1} Li_2SO_4	0–1.8 V	1 A g^{-1}	13 000	7*d*
SWCNTs	MnO_2@graphene	0.5 mol l^{-1} Na_2SO_4	0–1.5 V	2.2 A g^{-1}	5000	8*a*
AC nanofibers	MnO_2@graphene	1 mol l^{-1} Na_2SO_4	0–1.8 V	1.2 A g^{-1}	1000	8*b*
Graphene	Nanowires MnO_2@graphene	1 mol l^{-1} Na_2SO_4	0–2 V	5 A g^{-1}	1000	8*c*
AC	PbO_2	5.3 mol l^{-1} H_2SO_4	0.8–1.8 V	0.8 A g^{-1}	4500 (90%)	8*d*
AC	PbO_2 nanowires	0.1 mol l^{-1} CH_3SO_3H + 0.1mol l^{-1} $Pb(NO_3)_2$ + 4 mol l^{-1} $NaNO_3$	0–1.7 V	40C	5000 (100%)	9*a*
AC	$Ni(OH)_2$@CNTs	6 mol l^{-1} KOH	0–1.6 V	0.5 A g^{-1}	—	9*b*
AC	$LiCoO_2$ nanoparticles	0.5 mol l^{-1} Li_2SO_4	0–1.8 V	10 A g^{-1}	40 (100%)	9*c*
AC	$LiMn_2O_4$ nanorods	0.5 mol l^{-1} Li_2SO_4	0–1.8 V	10 A g^{-1}	1200 (>94%)	9*d*
AC	$LiMn_2O_4$ nanochains	0.5 mol l^{-1} Li_2SO_4	0–1.8 V	10 A g^{-1}	200 (100%)	10*a*
AC	Porous $LiMn_2O_4$	0.5 mol l^{-1} Li_2SO_4	0–1.8 V	90C	10 000 (93%)	10*b*
AC	$NaMnO_2$	0.5 mol l^{-1} Na_2SO_4	0–1.9 V	120 C	10 000 (100%)	10*c*
AC	$K_{0.27}MnO_2$	0.5 mol l^{-1} K_2SO_4	0–1.8 V	25 C	10 000 (100%)	10*d*

[a] The numbers indicate the cycling number and capacitance retention in the brackets, respectively.

• The ionic conductivity of aqueous electrolytes is high, about two orders of magnitudes higher than that of organic electrolytes,[4d] which ensures high rate capability and thus high specific power. In aqueous electrolytes, the bare electrode is exposed to the electrolyte in the absence of surface layer and the charge transfer occurs easily across the electrolyte/electrode interface without the impeding effect of the surface layer.

• Water is an ideal electrolyte solvent, in that the decomposition products, hydrogen and oxygen, will not contaminate the electrolyte. In addition, water can render the supercapacitors tolerant to overcharging by producing hydrogen and oxygen at the negative and positive electrodes, respectively.[4e]

• Hydrated ions are much smaller than those ions solvated by organic electrolytes, and their capacitance is much larger than for the organic electrolytes.

• As a result, even if the working voltage of aqueous electrolyte is low, it is of great promise for the aqueous ASCs to achieve higher energy and power densities.[2,5]

In this review, our main target is aqueous ASCs, and some characteristics are summarized in Table 2. The key to achieving high energy and power densities for aqueous ASCs is the development of appropriate electrode materials. Herein, a brief summary of the latest progress concerning their electrode materials is provided. A particular focus is directed to the preparation and electrochemical performance of various nanostructured electrode materials, which are advantageous to achieve high power density.[5a] Current challenges and future strategies of ASCs are also discussed.

2. Negative electrode materials for asymmetric supercapacitors

Negative electrode materials, which are sometime called anode materials, include carbonaceous materials (porous carbons, carbon nanotubes (CNTs) and graphene), oxides (V_2O_5, MoO_3), their composites and other materials.

2.1 Carbonaceous materials

Carbonaceous materials include porous carbons, carbon nanotubes (CNTs) and graphene, and their action mechanism is as eqn (3). Of course, they can also be used as positive electrode materials for ASCs. However, their action mechanism is different. As to other carbons such as carbon xerogels and carbon nanocages, they are just different in shape or morphology. Their action as negative electrode materials for ASCs is principally the same and they will not be specifically discussed here.[5a,5b]

$$\text{Carbon} + C^+ + e^- \leftrightarrow \text{Carbon/C} \quad (3)$$

Where C^+ and/represent cation and interface, respectively.

2.1.1 Porous carbons. Porous carbons mainly include activated carbons (ACs) and nanoporous carbons (NPCs). The characteristics and performances of carbons with controlled porosities for EDL-typed supercapacitors have been discussed in detail in some recent reviews.[5c,5d] However, most of these reports are directed for the use of nonaqueous electrolytes and carbons with controlled porosities and they will not be discussed here. Strictly speaking, AC also belongs to NPCs. However, AC has macropores and is differentiated from NPCs.

There are two methods to prepare ACs: physical and chemical activation. The former involves gasification of the carbon produced from carbonization with an oxidizing gas

Published on 16 avril 2013. Downloaded on 2024-08-15 14:15:36.

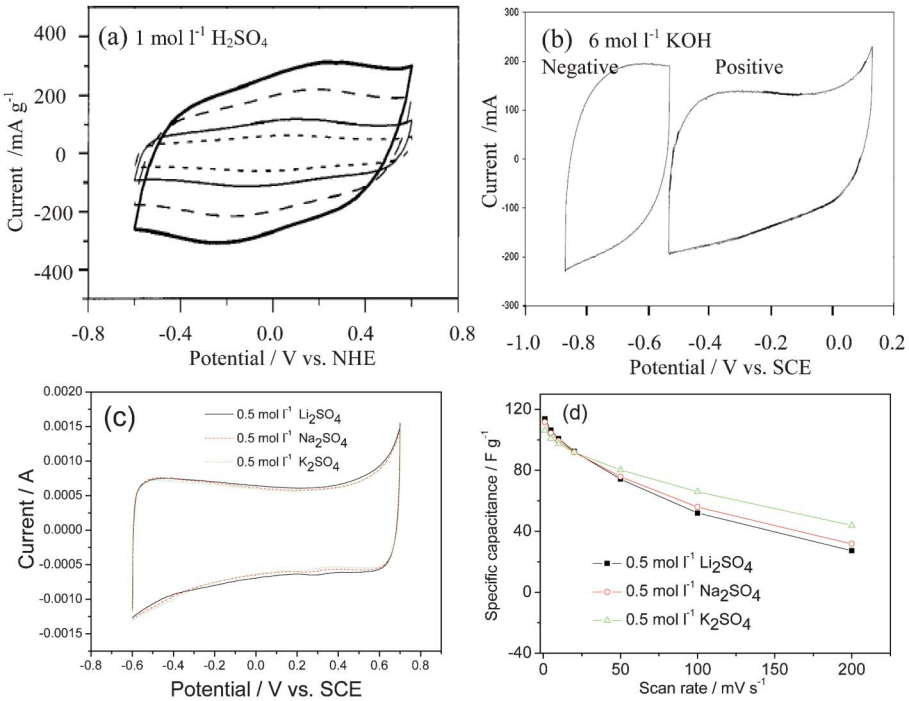

Fig. 2 CV curves of AC as negative electrodes in different aqueous electrolytes: (a), (b) (modified from ref. 12*b*), (c) 0.5 mol l^{-1} Li_2SO_4, Na_2SO_4 and K_2SO_4 solutions and (d) the change of capacitance with the scan rate in different aqueous electrolytes (modified from ref. 13). Note: Fig. 2b also shows that AC can also be positive electrodes.

such as air, CO_2 and water vapor at elevated temperatures. In the case of the latter, carbonization and activation are carried out by thermal decomposition of the precursor impregnated with a chemical activating agent, such as $ZnCl_2$, KOH, K_2CO_3, HNO_3 or H_3PO_4. Recently, some processes including laser ablation, electrical arc, chemical vapor decomposition (CVD) and nanocasting, which do not include activation processes, can also be used to prepare ACs.[5a] A variety of precursors are used for producing ACs such as charcoals (*i.e.* woods and coconuts), resins, petroleum coke, pitch and biomasses including waste paper.[6e]

Since the action mechanism for capacitance is mainly due to absorption/desorption, the specific surface area, porosity and functional groups of ACs are important factors to achieve high energy density, which are dependent on the nature of precursor, activating agent, and condition of the activation process. For instance, the solid product obtained from a specific raw material containing dominantly aromatic compounds (such as biomass-derived tar), is characterized by a dense structure and weak reactivity towards steam activation. On the contrary, the final carbon material prepared from a furfural precursor is less dense and more reactive, due to the insertion of oxygen in the carbon skeleton that favors the formation of pores during the activation process. The pores including micro-, meso-, and macro-pores in the ACs are randomly distributed.

In the case of NPCs, most are prepared by template methods so that the porosity and pore size can be tailored. For example, metal–organic frameworks (MOFs) such as $Zn_4O(OOCC_6H_4COO)_3$), silicas such as SBA-15, zeolites and oxides such as MgO can be used as templates. The pore size is dependent on the templates and the porosity is on the amount of the templates.[5a,6f]

Of course, the surface of carbonaceous materials can be modified by some methods such as oxidation and plasma treatment to introduce functional groups.

When a potential is applied to a porous carbon electrode, oppositely charged ions are absorbed on its pore surfaces and electric double-layers are formed, thereby electricity being stored, and they can be used for the non-Faradic side of ASCs.[11] Acid, alkaline and neutral solutions can be used as electrolytes (Fig. 2). Cyclic voltammograms (CVs) are typically rectangular and time-potential curves are linear. However, due to the existence of some surface functional groups such as –C–OH, –C=O, –COOH, which can take place in the redox reactions, as shown in eqn (4)–(6), to produce pseudo capacitance, the CV curves deviate from rectangular—as shown in Fig. 2.

$$-C-OH \leftrightarrow -CO + H^+ + e^- \quad (4)$$

$$-COOH \leftrightarrow -COO + H^+ + e^- \quad (5)$$

$$-CO + e^- \leftrightarrow -C-O^- \quad (6)$$

However, as the amount of the functional groups on the surface is low, it could not present strong redox peaks on CV curves. During the modification, oxidation for too long a timescale is detrimental for carbon materials since it could

 This journal is © The Royal Society of Chemistry 2013

Published on 16 avril 2013. Downloaded on 2024-08-15 14:15:36.

reduce the surface area and electronic conductivity of the carbons, and impair their capacitive performance.

The specific capacitance of ACs is determined by both the ratio of edge/basal orientation and the nature of the functional group on the surface.[12a] A higher percentage of edge orientation results in the higher double-layer capacitance and favors stronger bonding of surface functional groups.

Considering the pore sizes, their influence on capacitance is closely related to electrolytes. Pores larger than 0.5 nm are generally available for the electroadsorption of simple hydrated ions in aqueous solutions. The optimal pore size range for double layer capacitance of NPCs in aqueous H_2SO_4 is between 0.8 and 2.0 nm. It is suggested that the adsorption of desolvated cations by contacting walls of small micropores seems to be more possible.[5a]

In the case of the same AC material in acid (1 mol l^{-1} H_2SO_4) or alkaline (6 mol l^{-1} KOH) solutions, different capacitances will be achieved.[12b] In neutral solutions, the ion size will also present different behavior at different current or power densities. For example, in 0.5 mol l^{-1} Li_2SO_4, Na_2SO_4 and K_2SO_4 aqueous electrolytes,[13] the rate behavior of the AC improves in the order of $Li_2SO_4 < Na_2SO_4 < K_2SO_4$. This can be attributed to the different hydrated ionic radius of Li^+ (3.82 Å), Na^+ (3.58 Å) and K^+ (3.31 Å) contributing to their different charge densities and their different migration speeds.[14] The hydrated ionic radius of K^+ is the smallest and its ionic conductivity is the highest, consequently its access to the inner pores of AC is much easier than Na^+ and Li^+, and the relaxation time for the migration of the hydrated K^+ is the shortest at the high scan rate. In addition, the equivalent series resistance (ESR) values for the three electrolytes decrease in the order of $Li_2SO_4 > Na_2SO_4 > K_2SO_4$. As a result, K_2SO_4-based electrolyte exhibits the largest capacitance at the high scan rates. At the low scan rate, the capacity is mainly determined by the size of un-hydrated cations, which decreases in the order of $Li^+ > Na^+ > K^+$ (Fig. 2d).[13]

2.1.2 CNTs. CNTs have hollow tubes with diameters in the nanometer range and lengths usually at the micro scale. Based on the number of tube walls, CNTs can be classified into single-walled carbon nanotubes (SWCNTs) and multi-walled carbon nanotubes (MWCNTs).[15a] SWCNTs are usually 1–2 nm in diameter and tens of microns in length. The specific surface area can be as large as 2630 m^2 g^{-1}. MWCNTs are made of coaxial cylindrical carbon layers with an interlayer distance of 0.34–0.37 nm, which is a little larger than that of graphite (0.335 nm). CNTs have a narrow pore size distribution, high electrical conductivity and high stability.[15b] As to their preparation, there are several methods discussed in a number of reviews.[16a–d] Of course, their shape or morphology is versatile depending on the preparation process.

CNTs can be doped by nitrogen and oxygen like disordered carbons.[16e] Together with other kinds of carbon materials, composites such as core-shell structures can be prepared.[17a] The core and the sheath can be composed of aligned CNTs and network-like nitrogen-doped CNTs, respectively. These composite fibers are flexible and weavable with excellent mechanical and electronic properties, which make them very promising as a family of new and high-performance fiber-shaped negative electrodes for ASCs. Interestingly, macroscopic Ni-microfiber-supported CNT aerogels can also be developed with a better electronic conductive network.[17b]

The capacitive behavior of CNTs is similar to that of AC. In the case of the hetero-atoms doped CNTs, it exhibits pseudo-capacitance through a Faradic reaction in the framework or as functional groups on the surface,[17a] which is similar to the doping of N in carbon for anode materials of lithium ion batteries.[16e] Interestingly, macroscopic Ni-microfiber-supported CNT aerogels show high specific capacitance (up to 359 F g^{-1} at the scan rate of 1 mV s^{-1}) in a 5.0 mol l^{-1} KOH aqueous electrolyte solution due to the excellent ion diffusivity, high electronic conductivity and large mesopore surface area of this composite electrodes, in which the Ni microfiber network serves as current collector, CNTs as nano conducting wire and carbon nanotube aerogels as ion storage reservoir. The specific capacitance of the composite based on CNTs increases with the amount of carbon aerogel. In addition, the cycling performance is also satisfactory.[17b]

In both single and multi-walled CNTs, the electronic transport occurs over long tube ranges without electronic scattering and the network of large external small pores formed by the entanglement of the CNTs allows for fast solvated ion diffusion during charge and discharge processes. This property makes them successful at carrying high densities of currents without energy dissipation.[17c] As a result, in most cases CNTs are often used in the form of composites, and their preparation and electrochemical performance in aqueous electrolytes will be expounded in the corresponding sections.

CNTs exhibit properties amenable to capacitive energy storage with unique tubular porous structures and superior electronic properties, fast ion and electron transportation. However, the production costs of CNT-based supercapacitors still cannot meet acceptable performance[18] and great efforts are still needed on developing novel carbon-based supercapacitor electrode materials with an overall high performance.[19]

2.1.3 Graphene. Graphene, a one-atom-thick 2D single layer of sp^2-bonded carbon, has attracted increasing attention in recent years. It possesses a unique two-dimensional structure and excellent mechanical, thermal and electronic properties. The unique electronic and mechanical properties of graphene as well as possible large surface area have brought great interest to materials scientists,[20,21] and graphene as an electrode material for ASCs has attracted a considerable amount of interest in the field of clean energy devices.[22]

Graphene can be prepared by several kinds of methods: exfoliation and cleavage of natural graphite, chemical vapor deposition (CVD) and plasma enhanced CVD (PE-CVD), electric arc discharge, epitaxial growth on electrically insulating surfaces such as silicon carbide (SiC), un-zipping of carbon nanotubes (CNTs), solution-based reduction of graphite oxides and so on.[23] Chemical synthesis of graphene using graphite, graphite oxide (GO) or other graphite derivatives as starting materials can not only be scalable but also provide graphene with processibility and new functions.[24] Usually, GO is firstly prepared in large quantities from graphite by the Hummers method using $KMnO_4$ and sulfuric acid.[25] Because of their COO^- groups, the graphene oxide product can be purified by

Published on 16 avril 2013. Downloaded on 2024-08-15 14:15:36.

centrifugation and dialysis to remove aggregates and various inorganic impurities such as metal ions and acids. The obtained GO colloids can be subsequently stabilized with surface charges,[26a] or with ionic surfactants[26b] followed by reduction with hydrazine solution[26c] or by thermal treatments in hydrogen-rich atmospheres.[26d]

The properties of graphene can be greatly affected by the number of layers and the degree of surface reduction or oxidation. In general, single layer suspensions can contain up to five layers, denoted as few layers graphene (FLG).[27] It can also be physically- and/or chemically modified, which is summarized elsewhere.[28]

Graphene can also be activated to achieve ultraporous graphene as the negative electrode for ASCs.[29] Hydrogels of graphene can be prepared *via* hydrothermal reduction of graphene oxide dispersions followed by further reduction with hydrazine or hydroiodic acid, for example, by 50% hydrazine at 100 °C for 8 h.[30]

However, aggregation and restacking are still a major hurdle that limits graphene-based nanocomposites from realizing their full performance, which causes inferior ionic accessibility and electrochemical performance.[31] In order to solve this problem, a three-dimensional (3D) macroporous structure that consists of chemically modified graphene is obtained using polystyrene colloidal particles or MgO as a sacrificial template.[32a,32b] Although macroporous graphene structures have been developed through various templates, the templating process *via* porous MgO layers opens opportunities for the mass production of porous graphene at low cost and is useful for applications that need graphene as a bulk material.

Graphene can also form composites with other kinds of carbon such as graphene oxide platelets@carbon films,[33] graphene@MWCNT, and graphene oxide@MWCNT.[34] For example, the flexible graphene@MWCNT film is prepared through a flow-directed assembly technique from a suspension of graphene oxide and pristine MWCNTs following by the use of gas-based hydrazine to reduce the GO to graphene sheets.[34] This flexible film has a layered structure with MWCNTs homogeneously dispersed among the graphene nanosheets.

Another direction is the form composites with other electrochemically active materials such as polyaniline (PAn), and polypyrrole (PPy).[35a] PAn nanofibers are grafted onto graphene to obtain a novel graphene–PAn (GP) composite.[35b] A composite film of chemically converted graphene (CCG) and PAn nanofibers (PAn-NFs) has a layered structure, and PAn-NFs are sandwiched between CCG layers.[35c] An alternative and effective route to prepare conducting PAn-grafted reduced graphene oxide composite with highly enhanced properties is reported elsewhere.[35d] The resultant composite has fibrillar morphology with a room-temperature electronic conductivity as high as 8.66 S cm^{-1}. Nanoplatelet-like structure of the composites of PPy and graphene is facilely synthesized by an electrochemical method.[35e]

Graphene-based hydrogel reduced by 50% hydrazine at 100 °C for 8 h is a good electrode material with a high specific capacitance of 220 F g^{-1} at a current density of 1 A g^{-1}. Amazingly, this capacitance can be maintained for about 74% as the current density increased up to 100 A g^{-1}.[30] Furthermore, it displays a power density of 30 kW kg^{-1} and an energy density of 5.7 kW kg^{-1} at such high current density. It also shows a long cycling life along with about 92% capacitance retention after 2000 cycles at a current density of 4 A g^{-1}. This excellent performance is mainly due to the relatively high conductivity as well as the unique 3D macroporous structure of this graphene-based hydrogel. The 3D interpenetrating structures can provide a good solution to the issue of poor ionic and electronic transport in electrode materials, thereby resulting in high electrochemical performance.[32a] The enhanced specific capacitance is attributed to the improved surface area of 3D macroporous assembly and high electronic conductivity. The specific capacitances of the as-pyrolyzed and N-doped macroporous reduced graphene oxide (RGO) assemblies are 86.7 F g^{-1} and 103.2 F g^{-1} in 1 mol l^{-1} aqueous H_2SO_4 solution, respectively. The porous graphene can present a capacitance up to 255 F g^{-1} in 6 mol l^{-1} KOH.[32b]

The MWCNTs in the composite films can not only separate the graphene sheets, but also bridge the defects for electron transfer between the graphene sheets, which facilitate transportation of electrolyte ions and electrons into the inner region of the electrode. Thus, these flexible films have a high specific capacitance of 256 F g^{-1} at the current density of 0.1 A g^{-1} and a good rate capability (49% capacitance retention at 50 A g^{-1}). Moreover, after 2000 charge/discharge cycles, the specific capacitance still retains 97%, indicating promising potential of its application in ASCs.[34]

The graphene–PAn nanofiber composite has a high capacitance performance of 579.8 and 361.9 F g^{-1} at current densities of 0.3 and 1 A g^{-1}. The preserved specific capacitance of this composite after 200 charge/discharge cycles is 270 F g^{-1}, conserving 96% of its original capacitance (282 F g^{-1}).[35b]

The composite film of CCG and PAn nanofibers exhibits a high capacitance of 210 F g^{-1} at 0.3 A g^{-1}, and this capacitance can be maintained for about 94% (197 F g^{-1}) as the discharging current density increases from 0.3 to 3 A g^{-1}. Its cycling life is also greatly improved.[35c] The PAn-grafted RGO composite shows a capacitance of 250 F g^{-1} with good cycling stability.[35d] The PPy@graphene nanocomposite manifests a high capacitance of 285 F g^{-1} at a current density of 0.5 A g^{-1}. Moreover, it exhibits superior rate performance and cycling stability compared with graphene, PPy and PPy@GO.[35e]

Another composite of graphene oxide@MWCNT shows exceptional stability as electrodes due to the p–p interactions between the two carbonaceous materials.[35f] A maximum capacitance of 251 F g^{-1} is obtained from CV experiments at 5 mV s^{-1} and a total increase of 120.5% is recorded in 1000 cycles for the composite at a scan rate of 20 mV s^{-1} in 1 mol l^{-1} H_2SO_4. The MWCNTs can channel the electrical current to some preferential sites on the surface of GO resulting in a partial recovery of GO to RGO.

2.2 Oxides

There are very rare oxides for negative electrodes of ASCs, which mainly include V_2O_5 and MoO_3. As to other oxides such as Fe_2O_3,[36] there are very rare reports and they will not be discussed here.

 This journal is © The Royal Society of Chemistry 2013

Published on 16 avril 2013. Downloaded on 2024-08-15 14:15:36.

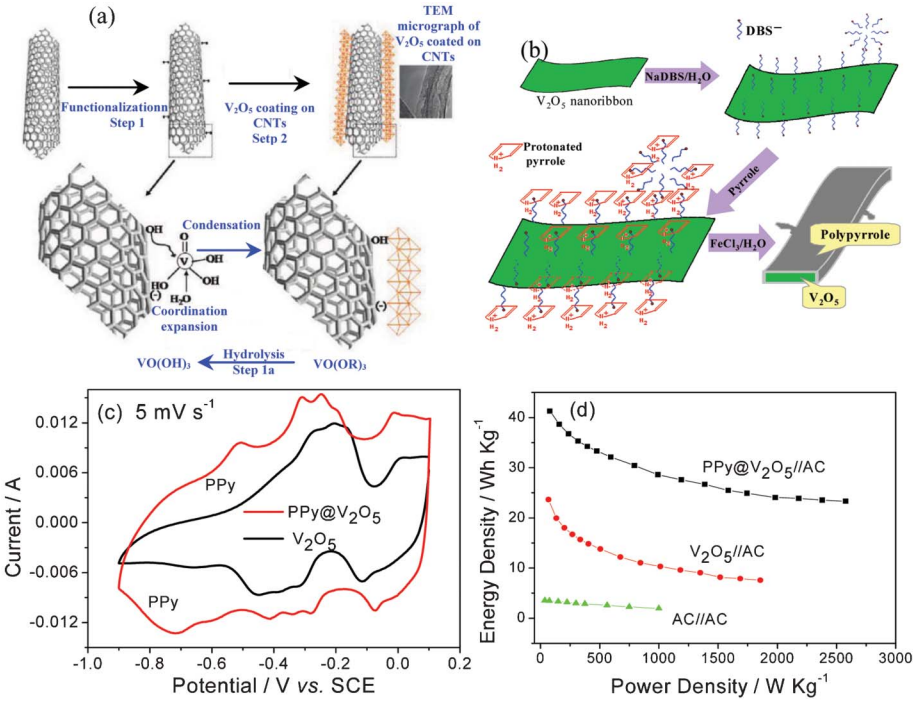

Fig. 3 Schematic illustration for the synthesis of (a) V_2O_5@CNTs (modified from ref. 37*a*) and (b) PPy@V_2O_5, (c) CV curves of V_2O_5 and PPy@V_2O_5 in 0.5 mol l^{-1} K_2SO_4 solution, and (d) Ragone plots of the ASC of V_2O_5//AC and PPy@V_2O_5//AC using 0.5 mol l^{-1} K_2SO_4 solution as the electrolyte (The capacitance and energy densities were calculated based on the total mass of two active electrode materials) (modified from ref. 6*b*).

2.2.1 V_2O_5. Vanadium pentoxide (V_2O_5) has been investigated as a positive electrode material for Li-ion batteries due to its lamellar structure, different oxidation states, high potential (about 3.0 V *vs.* Li/Li^+) and high capacity. It has been intensively studied for energy storage due to its high theoretical capacity and structural reversibility.[37–41] Its redox potential is also very wide, when it is lower than 0 V (*vs.* normal hydrogen electrode: NHE), it can act as a negative material for supercapacitors in aqueous electrolyte[42a] and its action mechanism is shown as the following eqn (7) and (8):

$$V_2O_5 + \delta M^+ + \delta e^- \leftrightarrow V_2O_{5-\delta}(OM)_\delta \quad (7)$$

$$V_2O_5 + \delta_H{}^+ + \delta e^- \leftrightarrow V_2O_{5-\delta}(OH)_\delta \text{ (when } M^+ \text{ cation is } H^+) \quad (8)$$

Of course, it can also be used as a positive electrode for ASCs, and will be expounded in the positive section.

V_2O_5 crystallizes with an orthorhombic layered structure belonging to the P_{mnm} space group with lattice parameters a = 11.510 Å, b = 3.563 Å and c = 4.369 Å. It is composed of distorted trigonal bipyramidal coordination polyhedra of O atoms around V atoms. In addition, V_2O_5 also exists in an amorphous phase.

The common methods to prepare nano V_2O_5 include a sol–gel process,[42b] which is the predominant and oldest one, quenching, hydrothermal in addition to other methods.[5a] The morphology and crystallinity of V_2O_5 are directly dependent on the as-used methods and conditions. For example, nanoparticles can be prepared by a precipitation process, nanoroll V_2O_5 by a ligand-assisted templating method, nanoporous V_2O_5 by a sol–gel method, and nanobelt $V_2O_5 \cdot 0.6H_2O$ *via* a hydrothermal process.[6a]

To improve its electronic conductivity, V_2O_5 is prepared with conductive agents such as CNTs and polypyrrole (PPy).[37] For example, V_2O_5-anchored CNTs are achieved as shown in Fig. 3a. Firstly, the functionalization of CNTs using concentrated nitric acid results in the modification of the CNT surface with functional groups like $-OH^-$, $-COO^-$, and –CO. These functional groups not only facilitate the dispersion of CNTs but also serve as centers for the polymerization and the condensation of vanadium oxy-trihydroxide formed during the slow hydrolysis of vanadium oxy-tripropoxide. Vanadium alkoxide ($VO(OR)_3$) hydrolyzes to vanadium oxytrihydroxide ($VO(OH)_3$) which undergoes coordination expansion with functional groups present on the CNT surface followed by condensation to V_2O_5 layers grafted on CNTs.[43] It can be further coated with PPy.[44] CNTs provide good support for the uniform distribution of vanadium pentoxides and a PPy layer of 10–12 nm thickness is fully coated on the V_2O_5/CNT.[44]

The growth of PPy on V_2O_5 nanoribbon surface is illustrated in Fig. 3b.[6b] V_2O_5 nanoribbons, which are prepared by hydrothermal treatment of NH_4VO_3 and poly(ethylene oxide)-*block*-poly(propylene oxide)- block -poly(ethylene oxide) copolymer in acid solution at 120 °C, are first ultrasonically dispersed in water dissolved with anionic surfactant dodecylbenzenesulfonate (DBS^-). When pyrrole is added, the pyrrole monomer adsorbs on the V_2O_5 surface *via* electrostatic interaction between anionic DBS^- and protonated pyrrole due to the acidic reaction system. Upon stirring the above

Published on 16 avril 2013. Downloaded on 2024-08-15 14:15:36.

mixture at 0 °C under N_2 flow, $FeCl_3$ solution is added dropwise to ensure the polymerization of pyrrole.

A nanocomposite of interpenetrating CNTs and vanadium pentoxide (V_2O_5) nanowires networks is synthesized *via* a simple *in situ* hydrothermal process.[43]

In the case of the virginal V_2O_5 nanowires, they exhibit four couples of reversible current peaks in the range of −0.9 − 0.1 V (*vs.* SCE) at the scan rate of 5 mV s^{-1} in 0.5 mol l^{-1} K_2SO_4 solution, signifying the redox reaction of V_2O_5 related to its variable V valence states (Fig. 3c). The assembled V_2O_5//AC ASC has an energy density of 23 W h kg^{-1} based on the total mass of two electrodes (Fig. 3d), higher than that for AC//AC capacitor.

The V_2O_5-anchored CNT composite is attractive for ASCs in 0.5 mol l^{-1} Li_2SO_4 solution due to its high specific capacitance. The ASC based on this nanocomposite exhibits an excellent charge/discharge capability, and high energy densities of 16 Wh kg^{-1} at a power density of 75 W kg^{-1} and 5.5 Wh kg^{-1} at a high power density of 3750 W kg^{-1}. In the case of the PPy@V_2O_5 electrode, besides the redox current characteristic of the V_2O_5 electrode (Fig. 3c), another couple of redox peaks appear at −0.70 and −0.50 V (*vs.* SCE), which can be designated to the undoping/doping process of PPy. The assembled PPy@V_2O_5//AC ASC using 0.5 mol L^{-1} K_2SO_4 solution as the electrolyte can be cycled reversibly from 0 to 1.8 V.[6b] This ASC exhibits excellent cycling behavior with no more than 5% capacitance loss after 10 000 cycles and their Coulombic efficiency remains about 100% except in the initial few cycles. The cycling behavior of PPy@V_2O_5 electrode is the best amongst the reported negative materials for ASCs. The main reason is that the PPy coating can effectively prevent the dissolution of the reduced vanadium ions and CNTs provide good electronic conductivity.[44] Moreover, the energy density of the PPy@V_2O_5//AC supercapacitor can be up to 42 W h kg^{-1}, almost twice as high as that of the V_2O_5//AC supercapacitor (Fig. 3d).

2.2.2 MoO_3. There are three basic polymorphs of MoO_3, *i.e.*, orthorhombic MoO_3 (α-MoO_3), monoclinic MoO_3 (β-MoO_3) and hexagonal MoO_3, in which α-MoO_3 is the thermodynamically stable phase. The α-MoO_3 phase possesses a unique layered structure: each layer is composed of two sublayers which are formed by corner-sharing [MoO_6] octahedra along [001] and [100] directions, and two sublayers are stacked together by sharing the edges of octahedra along the [001] direction. An alternate stacking of these layers along the [010] direction with van der Waals interaction leading to the formation of α-MoO_3 with a two-dimensional structure, which allows guest atoms, ions or molecules to be introduced between the layers through intercalation. It can accommodate up to 1.5 Li/Mo.[45]

To achieve good capacitive behavior, nanostructured materials such as nanoparticles, nanorods and nanoplates are prepared to favor the rapid charge and discharge process. Nanostructured molybdenum oxide can be prepared by potentiodynamic electrodeposition onto stainless steel. The deposit consists of particulates in the range of 30 to 80 nm.[46] Nanorod α-MoO_3 can be synthesized on a large scale by a hydrothermal method,[47] and MoO_3 nanoplates can be prepared by a sol–gel method very conveniently.[6c]

Composites of MoO_3 with carbon, graphene, other metal oxides, conducting polymers, have been prepared.[49] A highly uniform nanocomposite of MoO_3 and carbon with a weight ratio of 1 : 1 is prepared by a simple procedure of ball milling.[49b] ZnO@MoO_3 core/shell nanocables have been synthesized in large quantities by a simple electrochemical method at room temperature and the shell thickness of MoO_3 can be controlled by changing the deposition time.[48] A thin layer of PPy can be coated on MoO_3 nanoplates by the similar process to coat V_2O_5 nanowires,[6b] and the morphology of the PPy@MoO_3 composite is shown in Fig. 4a.

In terms of the electrochemical performance, it seems that the MoO_3 nanoplates exhibit the best performance among the nanoparticles, nanorods and nanoplates though they are tested in different solutions. The deposited MoO_3 nanoparticles present 477 F g^{-1} at 0.1 mA cm^2 in a solution of 0.005 mol l^{-1} H_2SO_4 and 0.095 mol l^{-1} Na_2SO_4 in the potential range of −0.3 − −0.55 V (*vs.* Ag/AgCl).[46] Nanorods synthesized at 180 °C exhibit a specific capacitance of 30 F g^{-1} at a scan rate of 5 mV s^{-1}, and remains 24 F g^{-1} at 100 mV s^{-1} in 1 mol l^{-1} H_2SO_4 solution in the potential range of −1.0–1.0 V (*vs.* Ag/AgCl). Its redox peaks are not symmetric. The anodic ones are mainly situated above 0.0 V (*vs.* Ag/AgCl), and the cathodic ones below 0.0 V (*vs.* Ag/AgCl).[47] MoO_3 nanoplates present higher capacitance than that of the bulk one in 0.5 mol l^{-1} Li_2SO_4 solution. The latter presents only one clear couple of redox peaks at −0.72/−0.6 V (*vs.* SCE) in its CV curve (Fig. 4b). As to the former, there are two couples of redox peaks at −0.39/−032 V and −0.75/−0.59 V (*vs.* SCE) (Fig. 4b), respectively. These peaks correspond to the reversible intercalation/de-intercalation of lithium ions into/out of the MoO_3 phase, and contribute to pseudocapacitance.

The nanocomposite of MoO_3 and carbon exhibits a higher capacitance than those of the pure milled graphite and MoO_3 in 3 mol l^{-1} KCl aqueous solution in the range of −0.5–0.5 V (*vs.* Ag/AgCl). This improvement is attributed to its unique structure, in which MoO_3 nanoparticles (with a size range of 1−180 nm) are uniformly dispersed in an electrically conductive carbon host.[49b] The ZnO@MoO_3 core/shell nanocomposites delivers a specific capacitance of 236 F g^{-1} at the scan rate of 5 mV s^{-1}, which is much larger than that of MoO_3 nanoparticles.[48] The nanocomposite of PPy@MoO_3 shows very good rate capability as shown in Fig. 4c, which is due to the conductive PPy coating. In addition, the coating can ensure a good cycling performance to prevent the dissolution of Mo ions.[49c]

When assembled into an ASC using AC as the positive electrode, as shown in Fig. 4d, the ASC can deliver a high energy density of 45 Wh kg^{-1} at 450 W kg^{-1}, and maintain 29 Wh kg^{-1} even at 2 kW kg^{-1}. In contrast, the energy density for the bulk MoO_3 is 32 Wh kg^{-1} at 450 W kg^{-1} and fades to 17.5 h kg^{-1} at 2 kW kg^{-1}. Evidently, this good rate behavior is due to the MoO_3 nanoplates. The average charge and discharge voltages for this ASC are about 1.10 and 0.95 V, respectively.[6c]

2.5 Other negative electrode materials

Other negative electrode materials include $Ru(OH)_2$, *n*-doped polymers such as PAn and PPy,[5a,16b,16c,50a] VN,[50b] and so on.

 This journal is © The Royal Society of Chemistry 2013

Published on 16 avril 2013. Downloaded on 2024-08-15 14:15:36.

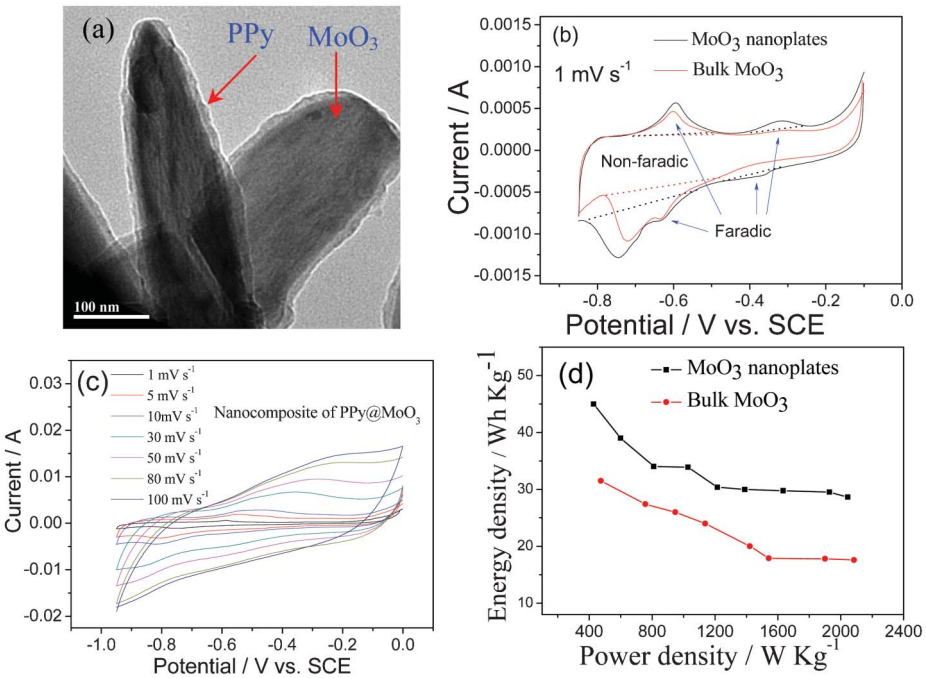

Fig. 4 (a) TEM micrograph of PPy coated MoO_3 nanorods, (b) CV curves of the bulk and nanoplates MoO_3, (c) CV curves of the PPy@MoO_3 nanocomposite at different scan rate and (d) Ragonne plot of the ASCs based on MoO_3//AC in 0.5 mol l^{-1} Li_2SO_4 solution (modified from ref. 6*c* and 49*c*).

$Ru(OH)_2$ can take place the following similar reactions as eqn (9):

$$Ru(OH)_2 \leftrightarrow RuO_\delta(OH)_{2-\delta} + \delta_H{}^+ + \delta e^- \quad (9)$$

It is sometimes called hydrous ruthenium oxide, mainly related to RuO_2, which is used as a positive electrode for ASCs, and this part will be expounded in the following 3.2.1 section.

As for conductive polymers such as PAn and PPy, their reaction mechanism is due to the *n*-doping of cations:

$$CP + e^- + C^+ \leftrightarrow CP^-C^+ \quad (10)$$

They have been studied widely, and some reviews can be referred.[5a,16c,16d] Since there is not much progress in this field, they will not be expounded here.

In the case of VN, it can produce pseudo-capacitance in acid, alkaline and neutral solutions. The main reason is the existence of surface nitride oxides (VN_xO_y), which can take place the following reactions:

$$2\ VN_xO_y + SO_4{}^{2-} + H_2O \leftrightarrow VN_xO_y/SO_4{}^{2-} + VN_xO_y{-}OH + H^+ + e^-\ (\text{acid}) \quad (11)$$

$$VN_xO_y + OH^- \leftrightarrow VN_xO_y/OH + e^-\ (\text{alkaline}) \quad (12)$$

$$VN_xO_y + NO_3{}^- \leftrightarrow VN_xO_y/NO_3 + e^-\ (\text{neutral}) \quad (13)$$

where "/" represents the electrical double layer.

The electrical double layer capacitance and pseudo-capacitance in 2 mol l^{-1} KOH and 0.5 mol l^{-1} H_2SO_4 electrolytes is greater than 1 mol l^{-1} $NaNO_3$ electrolyte. The main reason is due to the small sizes of OH^-. Their respective capacitance is 114, 273 and 45.7 F g^{-1}.[50b]

3. Positive electrode materials for asymmetric supercapacitors

In the present section we focus on the most recent work regarding the latest development on positive electrode materials for ASCs. Actually, as discussed above, carbonaceous materials like AC, CNT and graphene and oxides such as MoO_3 and V_2O_5 can also be used as negative electrode materials for ASCs. Particular attention in this section is paid to oxides such as RuO_2, MnO_2, MoO_3, V_2O_5, PbO_2 and cobalt oxides, $Ni(OH)_2$, intercalation compounds and other materials.

3.1 Carbonaceous materials

Carbonaceous materials mentioned in Section 2.1 including AC, porous carbons such as NPCs, CNTs and graphene can also be used as positive electrode materials for ASCs, and their action mechanism is as eqn (14):

$$\text{Carbon} + A^- \leftrightarrow \text{Carbon/A} + e^- \quad (14)$$

Where A^- and/refer to anion and interface, respectively.

Of course, acid, alkaline and neutral aqueous solutions can be used as electrolytes.[51] The parameters such as porosity, pore size and its distribution and functional groups are also crucial to affect their electrochemical performance, which will not be expounded further. The former discussion in 2.1

Published on 16 avril 2013. Downloaded on 2024-08-15 14:15:36.

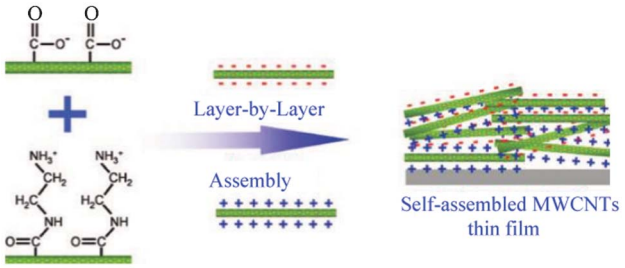

Fig. 5 Layer-by-layer assembled MWCNT thin film with positively and negatively charged MWCNTs (modified from ref. 52*a*).

section about their preparation can also be referred. Here just several examples are provided.

An AC can be prepared from the carbonization of resorcinol-formaldehyde resin with KOH as activation agent to present a high BET surface area of 1673 $m^2\ g^{-1}$ with a great number of micropores of a diameter less than 1.5 nm.[51*b*] Carbon materials can also form composites such as AC with CNTs.[51*c*]

MWCNT thin films with controlled thickness can be prepared by layer-by-layer (LBL) assembly of surface functionalized MWCNTs (Fig. 5).[52*a*] For example, negatively and positively charged MWCNTs are functionalized on their exterior walls with carboxylic acid groups[52*b*] and amine groups,[52*c*] respectively. By LBL assembly using their stable dispersions, MWCNT films consisting of well-dispersed MWCNTs can be achieved as shown in Fig. 5.

Graphene can be prepared by electrochemical reduction of graphene oxide instead of chemical reduction. The oxygen content is significantly decreased and the sp^2 carbon is restored.[52*d*]

In terms of the electrochemical performance of the carbon materials, the above AC with micropores of 1.5 nm shows good rate performance at the scan rates from 2 to 40 mV s^{-1}, which is shown in Fig. 6a. It presents higher specific capacitance, higher power density and higher energy density in comparison with the commercial activated carbon (Maxsorb: Kansai, Japan) as positive electrode for ASCs. Its specific capacitance is 500 F g^{-1} in 6 mol l^{-1} KOH electrolyte at a current density of 233 mA g^{-1}, which remains 302 F g^{-1} even at a high current density of 4.6 A g^{-1}. This is ascribed to well-developed micropores smaller than 1.5 nm, the presence of electrochemically oxygen functional groups and low equivalent series resistance.[51*b*]

For the LBL MWCNT thin films, they present an average capacitance of 159 F g^{-1} in 1.0 mol l^{-1} H_2SO_4 solution, which is considerably higher than those of vertically aligned CNTs and conventional CNT electrodes[53] due to the high CNT densities and well developed nanopores.[52*a*]

The composite of AC with CNTs shows a capacitance of 295 F g^{-1} at 0.125 A g^{-1} and decreases to 180 F g^{-1} at 100 A g^{-1} in the voltage range of −1–1 V in 2 mol l^{-1} H_2SO_4. CNT addition provides inter-particle spacing and bridging media leading to a reduction in the Warburg diffusion and electrical resistance. The composite shows superior stability, with no decay of specific capacitance after 10 000 cycles.[51*c*]

Graphene from the electrochemical reduction of GO exhibits a much higher electrochemical capacitance and cycling durability than CNTs and chemically reduced graphene. Their specific capacitances can be measured with cyclic voltammetry (20 mV s^{-1}) in the potential range of 0–0.9 V (*vs.* NHE) is 165, 86, and 100 F g^{-1}, respectively, in 0.1 mol l^{-1} Na_2SO_4 solution.[52*d*]

3.2 Oxides

3.2.1 RuO_2. Ruthenium oxide (RuO_2) has been widely investigated as an electrode material for supercapacitors. Hydrous RuO_2 is the most promising electrode material for supercapacitors due to its high specific capacitance, highly reversible redox reactions in a wide potential range and long cycling life.[54] It can also be a negative electrode of ASCs. Here our main work is on its use as a positive electrode.

RuO_2 usually exhibits two phases: a crystal phase (RuO_2, rutile phase) and an amorphous hydrous phase ($RuO_2{\cdot}xH_2O$). The annealing temperature is a key factor affecting the morphology, which exists usually in the form of the nanostructure such as nanoparticles, nanorods and nanofibers. High annealing temperature, for example from 300 to 800 °C, leads to the crystalline phase of RuO_2 and less water content, resulting in the change of the number of active reaction sites, as well as the electron and proton conductivity. Electronic conductivity of RuO_2 nanocrystals is balanced with the protonic conductivity of the ambient structural water when

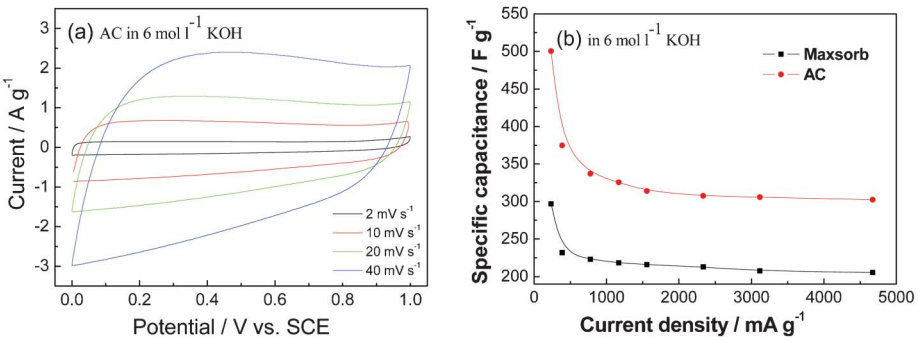

Fig. 6 (a) CV curves of an AC in 6 mol l^{-1} KOH aqueous electrolyte and (b) comparison of gravimetric capacitances against current density for the AC and the commercial Maxsorb carbon (modified from ref. 51*b*).

 This journal is © The Royal Society of Chemistry 2013

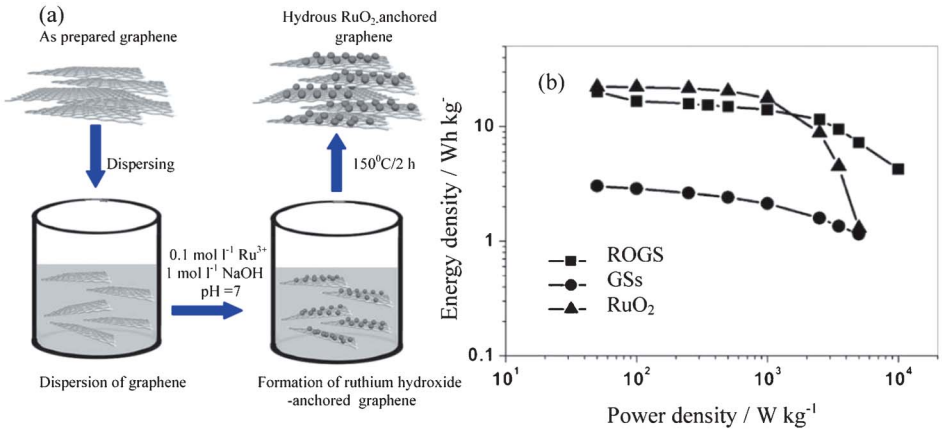

Fig. 7 (a) The preparation scheme of RuO_2/GSs composites (ROGS) and (b) Ragone plot for the as-prepared GSs, RuO_2, and ROGS (Ru, 38.3 wt%) (modified from ref. 59*a*).

Published on 16 avril 2013. Downloaded on 2024-08-15 14:15:36.

one mole of RuO_2 is hydrated by 0.58 mole of water ($RuO_2 \cdot 0.58H_2O$). Primary particulates will aggregate into secondary particles to form 3D framework porosity at above 200 °C. High specific surface area with nanoporous structure is also important to achieve high capacitance.[5a]

For positive electrode of ASCs, nanostructured RuO_2 is more attractive. It can be synthesized *via* various methods including potentiodynamic deposition, electrostatic spray deposition, chemical precipitation colloids, oxidative synthesis, hydrothermal synthesis, incipient wetness method, a combination of chemical vapor deposition (CVD), and electrolytic production.[5a] For example, 3D mesoporous architecture of $RuO_2 \cdot xH_2O$ nanotubular arrayed electrodes can be synthesized by anodic deposition technique,[54a] and thin-film RuO_2 electrodes are prepared by cathodic electrodeposition on a titanium substrate.[54b]

RuO_2 is the most promising electrode material, but the lack of abundance and the expensive cost of the precious metallic element (Ru) are drawbacks for commercialization of supercapacitors employing this element. As a result, and as an alternative material for pure RuO_2, many composites containing RuO_2 are synthesized by various methods.[5a] For example, the composites of amorphous $Ru_{1-y}Cr_yO_2/TiO_2$ nanotubes are synthesized by loading various amount of $Ru_{1-y}Cr_yO_2$ on TiO_2 nanotubes through a redox reaction of aqueous $K_2Cr_2O_7$ with $RuCl_3$. The 3D nanotube framework of TiO_2 offers a solid support for $Ru_{1-y}Cr_yO_2$ active materials, allowing the active material to be readily available for electrochemical reactions, and an increase in the efficient use of active materials. Different morphologies of RuO_2 can be prepared to get more efficient use of RuO_2. For example, core-shell structured RuO_2@VO_2 and RuO_2@TiO_2 nanotube can be prepared.[54c,54d] and anchored onto the surface of the GSs by strong chemical interactions between the residual oxygen-containing functional groups on the GSs and ruthenium hydroxide NPs, or by van der Waals interactions between the GSs and the NPs. Finally, to convert ruthenium hydroxide NPs into hydrous and amorphous RuO_2 NPs, annealing is carried out at 150 °C.[59a]

Of course, it can also form composites with carbon materials such as AC, CNT, NPC and graphene. For example, the RuO_2@AC composite can be synthesized by a sol–gel method on the surface of AC.[55] Ruthenium oxide@ordered mesoporous carbon composites materials can be prepared by impregnating an ordered mesoporous carbon, CMK-3, with $RuCl_3 \cdot xH_2O$ solution followed by annealing in nitrogen atmosphere.[56] CNTs acts as a support due to its good electronic conductivity and accessible surface textures, and RuO_2 can be dispersed on CNTs with different arrays.[52,57,58] Composites with graphene are prepared by combining a sol–gel process and low-temperature annealing. For example, as shown in Fig. 7a, at first, the solvent-free graphene sheets (GSs) are redispersed in a mixed solvent of ethanol and water, which leads to the release of the stacked sheets to give well-separated individual sheets. Then RuO_2 particles are anchored onto well-separated individual GSs during the sol–gel process, and the presence of water offers an aqueous medium (NaOH) for the formation of ruthenium hydroxide. Then ruthenium hydroxide nanoparticles (NPs) are formed by the reaction of $RuCl_3$ and NaOH.

The charge storage/delivery mechanism of $RuO_2 \cdot xH_2O$ can be presented in eqn (15) and (16).

$$RuO_x(OH)_y + \delta_H{}^+ + \delta e^- \leftrightarrow RuO_{x-\delta}(OH)_{y+\delta} \quad (15)$$

or simplified to:

$$RuO_2 + H^+ + e^- \leftrightarrow RuOOH \quad (16)$$

RuO_2 can present a very good rectangular shape in the CV curves. For example, the 3D mesoporous $RuO_2 \cdot xH_2O$ nanotubular arrayed electrode can retain this shape up to 1000 mV s^{-1} (Fig. 8a). Its capacitance does not fade much with the scan rate (Fig. 8b). It shows a specific power of 4320 kW kg^{-1} and specific energy of 7.5 Wh kg^{-1} in 1.0 mol l^{-1} H_2SO_4 solution at the potential range of 0–1.0 V (*vs.* Ag/AgCl), respectively.[54a] The specific capacitance and charge–discharge performance of the thin-film RuO_2 are dependent on the electrode thickness. The thinner the electrode thickness is, the higher the specific

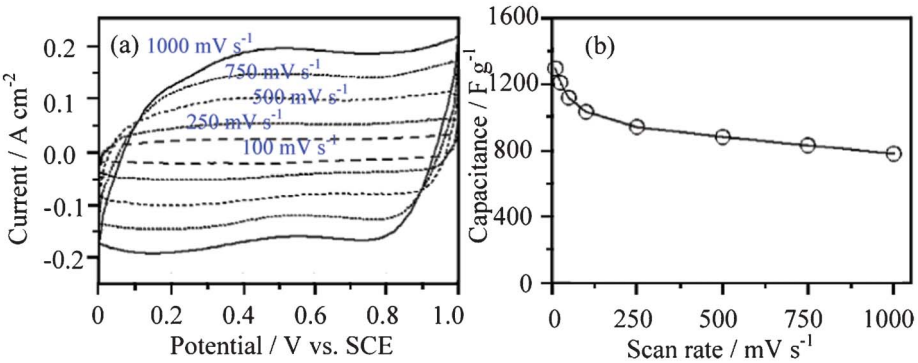

Fig. 8 (a) CV curves at different scan rates and (b) dependence of the capacitance on the scan rate for an annealed $RuO_2{\cdot}xH_2O$ nanotube arrayed electrode (0.19 mg cm^{-2}) in 1.0 mol l^{-1} H_2SO_4 solution (modified from ref. 54*a*).

Published on 16 avril 2013. Downloaded on 2024-08-15 14:15:36.

capacitance will be. For example, a maximum specific capacitance of 788 F g^{-1} is achieved with an electrode thickness of 0.0014 g cm^{-2} in 0.5 mol l^{-1} H_2SO_4 solution at the potential range of 0–0.6 V (*vs.* Ag/AgCl).[54*b*] The ASC with anthraquinone-modified carbon fabric as the negative electrode and RuO_2 as the positive electrode shows a maximum energy density of 26.7 Wh kg^{-1} in 1 mol l^{-1} H_2SO_4 solution in the voltage range of 0–1.3 V. It can arrive at an energy density of 12.7 Wh kg^{-1} at 0.8 A cm^{-2} discharge rate with average power density of 17.3 kW kg^{-1}.[59*b*]

A common method for increasing the electrochemical charge stored per RuO_2 is the addition of a second metal oxide, such as VO_2. In an acidic solution, specific capacitance exceeding 1200 F g^{-1} based on RuO_2 in 0.5 mol l^{-1} H_2SO_4 solution is obtained for $Ru_{0.35}V_{0.65}O_2$ in the potential range of 0.1–1.3 V (*vs.* NHE).[54*c*] The ASC consisting of AC as the negative electrode and a RuO_2@TiO_2 nanotube composite as the positive one has good electrochemical performance in 1 mol l^{-1} KOH solution in the voltage range of 0–1.4 V. The energy density reaches 12.5 Wh kg^{-1} at a power density of 150 W kg^{-1}. When the power density increases up to 1207 W kg^{-1}, its energy density decreases to 5.7 Wh kg^{-1}. The ASC also exhibits a good cycling performance and keeps 90% of initial capacity over 1000 cycles.[6*d*] The $RuO_2{\cdot}xH_2O$@TiO_2 nanocomposite exhibits weakly mass-dependent specific capacitance and high-power capacitive characteristics in comparison with pure $RuO_2{\cdot}xH_2O$.[54*d*]

The nanocomposite of RuO_2 with carbon materials can achieve both high power and high energy density with low cost no matter whether it is in acid or alkaline solutions.[55,56,58,59] For example, RuO_2 electrodeposited on a highly porous SWCNT film can show a maximum specific capacitance of 1715 F g^{-1} based on the weight of RuO_2,[58*d*] which is closely approaching the theoretical maximum capacitance (2000 F g^{-1}). Ruthenium oxide@ordered mesoporous carbon (CMK-3) has a higher specific capacitance due to the high specific surface area of the mesoporous carbon and the pseudo-capacitance of amorphous RuO_2.[56] However, the electrochemical performance of most porous carbon-based electrodes is limited by the surface area blocked by the loaded RuO_2 particles that may not be accessible by the aqueous electrolyte used; therefore the advantages of high-surface-area carbon-based double-layer capacitance cannot be fully utilized in these composites. As a result, RuO_2@graphene sheets (GSs) composites perform much better than other RuO_2@carbon composites in terms of the absence of pore blockage during the RuO_2-loading process and the anchoring of fine RuO_2 particles uniformly on the surface of conducting GSs (Fig. 7b).[59*a*] The RuO_2@GS composite exhibits high specific capacitance (570 F g^{-1} for 38.3 wt% Ru loading), enhanced rate capability, excellent electrochemical stability (97.9% retention after 1000 cycles), and high energy density (20.1 Wh kg^{-1}) at low charge/discharge current rate (100 mA g^{-1}).[59*a*]

3.2.2 MnO_2. MnO_2 has attracted much attention for applications in supercapacitors owing to its environmental compatibility, low cost, and abundant availability on earth, which functions as positive of ASCs as eqn (17):

$$MnO_2 + \delta M^+ + \delta e^- \leftrightarrow MnO_2/M_\delta \tag{17}$$

Up to now, several crystallographic phases of MnO_2, *i.e.*, ramsdellite-, α-, β-, γ-, δ-, and λ- phases have been reported according to the different linking manner of [MnO_6] octahedral, and their different crystalline phases are described by the size of the tunnel formed with the number of octahedra subunits ($n \times m$), and the tunnel type as well as size is presented in Table 3.[5*a*]

Nanostructuring and forming composites with a high surface area and conductive matrix are the two major strategies to improve the poor electronic conductivity of MnO_2 in the development of high-performance MnO_2-based electrodes for supercapacitors applications.[60*a*]

The crystallographic structure and morphology of nanostructured MnO_2 are greatly dependent on synthetic factors

Table 3 Tunnel size of different crystallographic phases of MnO_2

Crystallographic form	Tunnel type	Tunnel size (Å)
ramsdellite	(1 × 2)	2.3
α	(1 × 1), (2 × 2)	1.89, 4.6
β	(1 × 1)	1.89
γ	(1 × 1), (1 × 2)	1.89, 2.3
δ	Interlayer distance	7.0

 This journal is © The Royal Society of Chemistry 2013

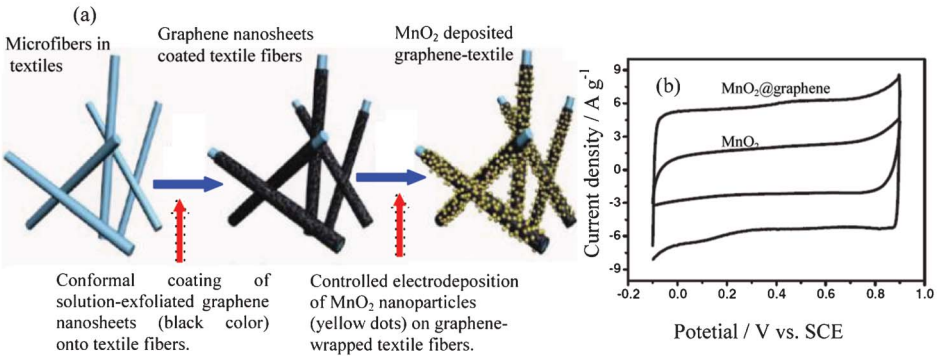

Fig. 9 (a) Schematic illustration of two key steps for preparing hybrid MnO_2-nanostructured textiles@graphene and (b) CV curves of an optimized MnO_2@graphene at different potential windows at the scan rate of 20 mV s^{-1} in 1 mol l^{-1} Na_2SO_4 solution (modified from ref. 8*a* and 8*b*, respectively).

Published on 16 avril 2013. Downloaded on 2024-08-15 14:15:36.

such as the pH value, concentration of inorganic cation templates and potential. [5a,61] Porous MnO_2 (pore size *ca.* 5–30 nm) can be prepared by an organic–aqueous interfacial method. The surface area and pore size distribution of MnO_2 can be controlled by adjusting the reaction time and the content of surfactant in the aqueous phase. High surface area mesoporous MnO_2 with an α-phase crystalline structure has been synthesized by the reduction of potassium permanganate with ethylene glycol under acidic conditions.[5a] Hydrothermal or solvothermal synthesis is another important method to prepare nanostructured MnO_2.[61] A simple hydrothermal process based on $KMnO_4$, sulfuric acid and Cu scraps can prepare α-MnO_2 hollow spheres and hollow urchins. The hollow sphere or urchin structured α-MnO_2 materials possess a highly loose, mesoporous cluster structure consisting of thin plates or nanowires.[62a]

In the case of the composites of MnO_2 with other materials, most of the latest reports are related to carbonaceous materials such as carbon aerogels,[63] AC,[7b,64] CNTs and graphene. Formerly there are a few reports on their composites with conductive polymers,[16c] which will not be expounded upon here. Mesoporous MnO_2 can be deposited on AC to achieve a composite.[7b,64] Zn_2SnO_4@MnO_2 core/shell nanocable-carbon microfiber composites are fabricated as follows: the crystalline Zn_2SnO_4 nanowires grown radially on carbon micro fibers (CMFs) are uniquely serve as highly electrical conductive cores to support redox active MnO_2 shells with a highly electrolytic accessible surface area and provide reliable electrical connections to the MnO_2 shells, enabling full utilization of MnO_2 and fast electronic and ionic conduction through the electrode.[65] As formerly mentioned, CNTs present higher electronic conductivity than AC, and there are quite some composites of CNTs with MnO_2.[7d,8,57,66–68]

For example, the composites of MnO_2 nanowires with MWCNTs can be easily prepared by a hydrothermal method.[7d] A binder-free MnO_2@CNT array electrode with hierarchical porous structure, high surface area and superior conductivity is fabricated by combining electrodeposition and a vertically aligned CNT array framework.[66]

Amorphous or poorly crystalline MnO_2 nanoparticles can be deposited onto ultraporous activated graphene from $KMnO_4$ solution.[29] A solution-phase assembly can be used to prepare a composite of MnO_2 nanowires@graphene sheets.[8c] Graphene can be decorated with flower-like MnO_2 nanostructures by electrodeposition to achieve a composite.[69] The graphene@MnO_2-textile composite can be prepared by the process shown in Fig. 9a. Firstly, the highly porous textile fibers are coated by graphene nanosheets (GNSs) that are prepared *via* a facile solution-based exfoliation process. The coating is done by a simple "dip and dry" process, which is similar to that widely used in the textile industry for dyeing fabrics and fibers. The second is the controlled deposition of MnO_2 nanomaterials on the as-prepared conductive textile fibers. Uniform deposition of MnO_2 nanomaterials is achieved on the surfaces of individual microfibers over almost the entire network of the porous textiles. Moreover, electrodeposited MnO_2 particles show a nanoflower-shaped hierarchical architecture and a clear interface between the MnO_2 nanoflower and the underneath GNSs.[8a] Conductive polymers can be further coated on MnO_2@MWCNTcomposites.[66,67] Other kinds of conductive matrix can also be a support for MnO_2 such as Zn_2SnO_4,[70] TiN[71] and nanoporous gold.[72,73]

MnO_2 can be used in acid,[29] alkaline and neutral solutions such as KCl,[60] Li_2SO_4,[61] Na_2SO_4[8c,69] and K_2SO_4,[61] and redox peaks in mostly rectangular CV curves can be observed (Fig. 10a). The redox peaks are related to the intercalation and de-intercalation of cations, which has been completely proved by X-ray photonic spectroscopy (XPS). At the current density of 0.2 A g^{-1}, the binding peak of O_{1s} from XPS analysis shifts significantly to a higher energy of 531.0 eV after the first discharge in Li_2SO_4 solution, which is ascribed to the intercalation of Li^+ ions into the MnO_2 lattice since Li–O coordination has a higher O_{1s} binding energy of 531.3 eV. The binding energy peaks of Mn_{2p} in the MnO_2 electrode shift slightly toward lower position after discharge, which is due to the valence transformation of Mn^{4+} to Mn^{3+}.[7c]

The pH affects the stable working potential of MnO_2 and the widest stable electrochemical window is achieved at pH $\approx$ 6.4 in the range of 6.4–10.[60c] The morphology and surface area of the prepared MnO_2 present great influence on the specific capacitance. [61,74–76] For example, the specific capacitance obtained from the electrochemically oxidized manganese films having hydrated and porous structure is generally higher than those from thermally oxidized samples.[74,75] The MnO_2

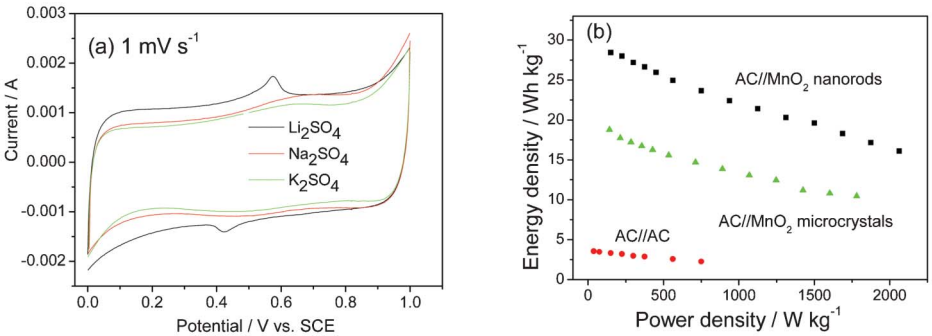

Fig. 10 (a) CV curve of MnO_2 in 0.5 mol l^{-1} different neutral electrolytes and (b) Ragone plots of the hybrid supercapcitors AC//MnO_2 nanorods, AC//MnO_2 microcrystals supercapacitor and AC//AC supercapacitor in 0.5 mol l^{-1} K_2SO_4 electrolyte (modified from ref. 7*c*).

Published on 16 avril 2013. Downloaded on 2024-08-15 14:15:36.

nanorods show much higher energy density than that of the micrometer one.[7c] MnO_2 nanoflowers can also be coated on $Ni(OH)_2$ nanoflakes.[62b]

Similar to carbonaceous materials as negative electrodes,[9a] different ions will show different capacitance. Just as shown in Fig. 10a, the MnO_2 nanorods have the largest capacitance (201 F g^{-1}) in Li_2SO_4 solution at the slow scan rates since the reversible intercalation/de-intercalation of Li^+ in the solid phase produces an additional capacitance besides the capacitance based on the absorption/desorption reaction. At the fastest scan rates they show the largest capacitance in the K_2SO_4 solution due to the smallest hydration radius of K^+ and the highest ionic conductivity of the solution.[7c]

Formerly, it was reported that the oxygen in the solution would affect the cycling life of MnO_2.[7a] However, if MnO_2 exists in the nanorods with a low crystallinity, the oxygen does not influence the cycling life. For example, after 23 000 full cycles, there is no clear evidence of capacitance fading.[7c]

After forming composites with conductive materials, the movement of electrons is greatly improved, leading to an enhancement of the capacitance and rate capability. For example, the binder-free MnO_2@CNT array composite shows excellent rate capability (50.8% capacity retention at 77 A g^{-1}) and high capacitance (199 F g^{-1} and 305 F cm^{-3}).[66] The PAn@MnO_2-MWCNTs composite delivers remarkably enhanced specific capacitance and cycling stability compared to MnO_2-MWCNTs, where the highest specific capacitance (350 F g^{-1}) is obtained at a current density of 0.2 A g^{-1}, higher than 92 F g^{-1} for pristine MWCNTs and 306 F g^{-1} for MnO_2-MWCNTs.[67] Hierarchical MnO_2 nanospheres@CNTs@conducting polymer ternary composite achieves a specific capacitance of 427 F g^{-1} in 1 mol l^{-1} Na_2SO_4 solution.[70]

The incorporation of graphene into the composites can provide them with the unique properties of graphene and also possibly induce new properties and functions based on synergetic effects. Fig. 9b shows the comparison of the CV curves for the MnO_2@graphene composite and the virginal MnO_2 in 1 mol l^{-1} Na_2SO_4 aqueous solution at 20 mV s^{-1}. The specific capacitance of the composite is evidently much higher than that of the virginal MnO_2.[8b] In neutral solution such as 1 mol l^{-1} KCl, the specific capacitance for the composite of nanoflower MnO_2 with graphene is 328 F g^{-1} at the potential range of 0–0.9 V (*vs.* Ag/AgCl), much higher than those of the graphene and MnO_2.[69] In 1 mol l^{-1} H_2SO_4 solution, the composite of MnO_2 nanoparticles with ultraporous activated graphene exhibits a specific capacitance of 175 F g^{-1} on the basis of the total mass of active materials of the positive and negative electrodes at a current density of 0.25 A g^{-1}.[29]

In the case of the MnO_2 nanowires@graphene composite, the nanostructured MnO_2 can prevent the aggregation of graphene sheets caused by van der Waals interactions, consequently leading to an increase in the available electrochemical active surface area and a suitable porous structure for energy storage.[8c] The graphene@MnO_2 composite is a flexible film and achieves a high specific capacitance (372 F g^{-1}) with excellent rate capability without the need of current collectors and binders.[77a] The unique characteristics of the MnO_2@graphene nanostructured textiles make them promising candidates for high-performance ASC electrode materials: 1) 3D porous micro structure of the polyester textiles allows conformal coating of GNSs and subsequent loading of MnO_2 and facilitates easy access of electrolyte ions to electrode surfaces; 2) the graphene nanosheet coating serves as high-surface-area, conductive paths for the deposition of MnO_2, providing excellent interfacial contact between MnO_2 and graphene for fast electron transport; 3) nanoflower architecture of the electrodeposited MnO_2 offers large electrochemically active surface areas for charge transfer and reduced ion diffusion length during the charge/discharge process.[8a]

In the case of composites of MnO_2 with other conductive materials, their electrochemical performance is also greatly improved. In the case of the MnO_2@Zn_2SnO_4 composites, the mass loading of MnO_2 can be up to 60% and it still shows a capacitance as high as 200 F g^{-1} including excellent charge/discharge rate and cycling stability.[65] The coaxial array of MnO_2@TiN nanotube composite shows a capacitance of 681 F g^{-1} at a current density of 2 A g^{-1} and excellent rate capability (267.2 F g^{-1} at a impressing scan rate of 2000 mV s^{-1}) in1 mol l^{-1} Na_2SO_4 solution due to the electronic conducting TiN framework.[71] The MnO_2@nanoporous gold composite can show a surprising high specific capacitance (about 1145 F g^{-1}) that is close to the theoretical value.[73]

In the case of the ASCs, different negative electrodes can be used. The active material weight ratios (positive to negative),[77b] voltage window[77c] and different aqueous electrolytes[61] will affect the performance of the assembled ASCs. As shown in

 This journal is © The Royal Society of Chemistry 2013

Published on 16 avril 2013. Downloaded on 2024-08-15 14:15:36.

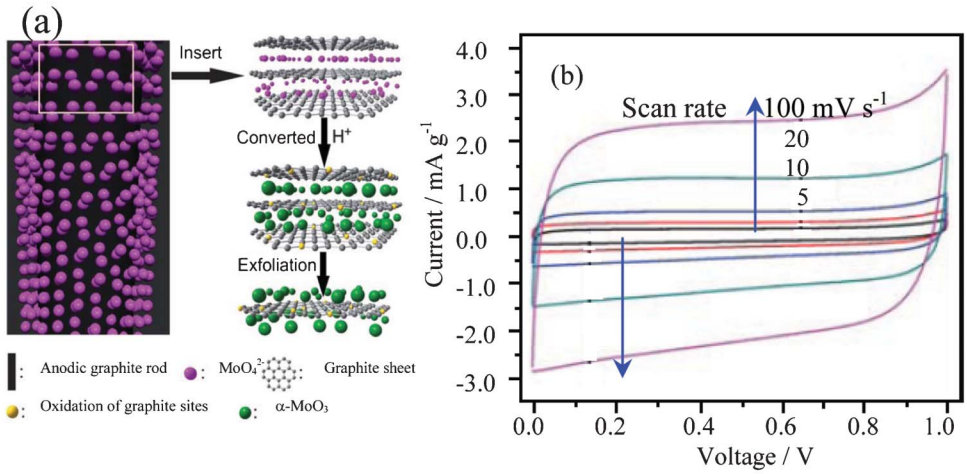

Fig. 11 (a) Illustration of the formation of the composite of α-MoO_3-decorated graphene sheets by electrolytic exfoliation from graphite with the assistance of molybdate and (b) CV curves of the composite in 6 mol l^{-1} KOH (modified from ref. 49*a*).

Fig. 10b, the ASC of AC//MnO_2 nanorods can have higher energy density and better rate capability than that of AC//MnO_2 micrometer.[7c] When MWCNTs are introduced into MnO_2 nanowires, their rate capability is very good. The energy density of the ASC of AC//MnO_2 nanowires@MWCNTs stays almost constant with an increase of power density even at 3340 W kg^{-1}.[7d] Moreover, the capacity of this ASC does not change much after 13 000 cycles even when oxygen is not removed.[7d] In 1 mol l^{-1} H_2SO_4 solution, the ASC of graphene//MnO_2 nanoparticles@graphene can operate up to 2 V. Its energy density can be 24.3 Wh kg^{-1} (at a power density of 24.5 kW kg^{-1}) and power density be 32.3 kW kg^{-1} (at an energy density of 20.8 Wh kg^{-1}).[29] A capacitance retention of 80.5% over 5000 cycles is achieved for this device.[29] In 1 mol l^{-1} Na_2SO_4 solution, the ASC based on graphene//MnO_2 nanowires@graphene can be reversibly cycled in the high-voltage range of 0–2.0 V and exhibits an energy density of 30.4 Wh kg^{-1}, which is much higher than those of symmetric supercapacitors based on graphene//graphene (2.8 Wh kg^{-1}). Moreover, it has a high energy density of 7.0 Wh kg^{-1} even at a power density of 5000 W kg^{-1} and presents an acceptable cycling performance.[8c] However, the ASC of graphene//MnO_2 nanowires@graphene presents a little worse cycling performance (79% retention after 1000 cycles) compared to AC//MnO_2 nanowires@MWCNTs and graphene//MnO_2 nanoparticles@graphene. When AC nanofibers are used as the negative electrode and the composite graphene@MnO_2 as the positive one, an energy density of 51.1 Wh kg^{-1} can be obtained for this ASC.[8b]

These results are encouraging and represent significant progress toward high-energy and safer ASC devices at low cost.

3.2.3 MoO_3. Since MoO_3 has a wide redox potential,[47,77d] it can also be a positive electrode materials for ASCs. Its structure and preparation can be seen from Section 2.2.2. Since its redox behavior at high potential is not good, it is modified to form composites with conductive materials such as graphite and graphene.[49a,49b] As shown in Fig. 11a, the composite of MoO_3@graphene sheets is prepared by electrolytic exfoliation from graphite with the assistance of molybdate. During the electrochemical reaction process, the anions of MoO_4^{2-} move to the positive graphite electrode under the influence of an applied electric field and insert into the graphite layers, which subsequently are converted to MoO_3 nanoparticles under strong acid conditions, leading to the electrolytic exfoliation of the graphite rod. At the same time, anodic oxidation of water produces hydroxyl and oxygen radicals. These radicals can result in hydroxylation or oxidation of graphite and the dissolution of carbon nanocrystals from the anode. These processes occur initially at edge sites, grain boundaries, or defect sites.[49a] This electrochemical method for the synthesis of α-MoO_3-decorated graphene sheets with just a one-step treatment and with the assistance of molybdate is very efficient.

In neutral or alkaline solutions, the redox peaks are not clear (Fig. 11b).[49a,49b] In acid solutions such as 1 mol l^{-1} H_2SO_4, the redox peaks can be clearly identified.[49b] After the heat treatment at 200 °C, the composite of MoO_3@graphene sheets can exhibit a high specific capacitance, up to 86.3 F g^{-1}, in the voltage range of 0–1 V in 6 mol l^{-1} KOH solution due to very high electronic conductivity (up to 5367 S m^{-1}).[49b]

3.2.4 V_2O_5. In the former Section 2.2.1, V_2O_5 and hydrous V_2O_5 as negative electrode materials have been discussed. However, they can also be used as positive electrode materials for ASCs in aqueous solution.[43] Some preparation methods for the negative electrode can also be used for the positive electrode. For example, a highly porous layered V_2O_5 can be prepared by sol–gel method.[78a] A V_2O_5 xerogel can be obtained by dissolving crystalline V_2O_5 in hydrogen peroxide and drying at elevated temperature.[78b] This xerogel V_2O_5 contains sheets comprised of two vanadium oxide layers with all the vanadyl bonds on the outside leading to a distorted octahedral structure around the lithium.

Electrospinning, regarded as a simple, one-step, cost effective method, is preferred over the other processes in synthesizing nanofibers with diameters ranging from tens nanometres to several micrometres.[79a] Furthermore, the

Published on 16 avril 2013. Downloaded on 2024-08-15 14:15:36.

structure, surface morphology and diameter of the fibers can be easily controlled by adjusting the variables of the electrospinning method, such as the applied potential, precursor concentration and flow rate of the solution. It is used to prepare V_2O_5 nanofibers (VNF).[79b] Hydrothermal and templates methods can be used to prepare nanobelts, nanorolls and nanoporous V_2O_5.[6a,78a,79c]

Conductive materials are also introduced to modify V_2O_5. For example, using arc-ion plating under Ar gas flow, a composite of V_2O_5@CNTs is achieved.[80a] A composite based on V_2O_5@SnO_2@CNT is prepared by a hydrothermal method in an autoclave.[80b] Highly ordered mixed V_2O_5@TiO_2 nanotubes can be formed by self-organizing anodization of Ti–V alloys.[80c]

Amorphous vanadium oxide prepared by quenching V_2O_5 fine powder heated at 950 °C for 30 min into a bath of deionized water has a specific capacitance of 350 F g^{-1} in KCl and the pH of electrolyte affects the potential window and capacity obviously.[5a] V_2O_5 usually has a higher capacitance in KCl solutions than that in NaCl or LiCl ones. In neutral 2 mol l^{-1} KCl electrolytes, maximum capacitance of 214 F g^{-1} for the porous V_2O_5 is obtained from CV at the scan rate of 5 mV s^{-1} in the voltage range of −0.2–0.7 V (*vs.* SCE).[78a,78b] For the electrospun V_2O_5 nanofibers, they yield a maximum capacitance of 190 F g^{-1} in neutral KCl solution.[79b] The $V_2O_5 \cdot 0.6H_2O$ nanobelts show four distinct couples of redox peaks in the potential range of 0–1.0 V (*vs.* SCE) in 0.5 mol l^{-1} K_2SO_4 (Fig. 12a). The redox peaks of $V_2O_5 \cdot 0.6H_2O$ electrode in K_2SO_4 can be ascribed to the intercalation/de-intercalation of K^+ ions into/from$V_2O_5 \cdot 0.6H_2O$ lattice accompanied with the electrochemical conversion of V^{5+} to different valence states. Its specific capacitance can be up to 180.7 F g^{-1} at 2C.[6a]

In the case of the composites, for example, the specific capacitance of the composite of V_2O_5@mesoporous carbon is increased by 61% in 1 mol l^{-1} KNO_3 solution comparing with that of the virginal mesoporous carbon.[80a] The electrochemical performance of V_2O_5@CNTs is significantly improved as compared with those of the bare oxide films and virginal CNTs. The CNTs covered with uniformly dispersed oxides lead to a significantly improved capacitive performance, as compared with the bare oxide films.[80b] The SnO_2–V_2O_5–CNT nanocomposite presents a capacitance of 121.4 F g^{-1} at 100 mV s^{-1} in 0.1 mol l^{-1} KCl solutions.[80c] The higher specific capacitance of V_2O_5@SnO_2@CNT demonstrates that the electronic properties can be changed favorably with a suitable choice of the additive in the electrode material.[80c]

The specific capacitance of the V_2O_5@TiO_2 nanotubes can reach to 220 F g^{-1} which is stable during cycling. The supercapacitive behavior can be ascribed to the V^{4+}/V^{5+} redox switching of the V_2O_5 phase embedded in the TiO_2 matrix. The good cycling stability of the mixed V_2O_5–TiO_2 nanotube arrays is due to the highly ordered 3D TiO_2-stabilized V_2O_5 nanotube structure which restrains the strain during ion intercalation.[80d]

The ASC consisting of AC//$V_2O_5 \cdot 0.6H_2O$ presents a stable voltage between 0 and 1.8 V (Fig. 12b). It delivers an energy density of 29.0 Wh kg^{-1} based on the total mass of the active electrode materials, a very good rate behavior with energy density of 20.3 Wh kg^{-1} at power density of 2000 W kg^{-1}, and also a rather good cycling performance.[6a] The species of aqueous electrolyte, current density, potential range and the active mass ratio of AC to V_2O_5 have great effect on the capacitive performance of the ASC. When the mass ratio of AC to V_2O_5 is to 3 : 1, the capacitance of the AC//V_2O_5 ASC is similar to that of the V_2O_5//V_2O_5 symmetric supercapacitors.[79d]

However, the cycling performance of V_2O_5 is still needed to improve due to the dissolution of V into the aqueous electrolytes leading to capacity fading, which is an urgent problem to be solved.

3.2.5 PbO_2. Lead dioxide (PbO_2) has been widely used as a positive electrode material of lead-acid batteries. The ASC of AC//PbO_2 in sulfuric acid system is considered more economically viable to replace the negative electrode of Pb in a lead acid battery, it presents an improved performance in terms of power and lifespan over the lead acid battery.[81a]

As a surface reaction, the redox activity of the PbO_2 relates to the morphology and structure (α-PbO_2 or β-PbO_2) and its electrochemically active surface area should be increased as the positive electrode of an ASC. It has been recognized that porous structured PbO_2 should present more electrochemical activities. As a result, thin film, porous and nanostructured PbO_2 have been prepared and different substrates have been investigated.[81b,82] For example, highly ordered macroporous films of both α-PbO_2 and β-PbO_2 are prepared by electro-

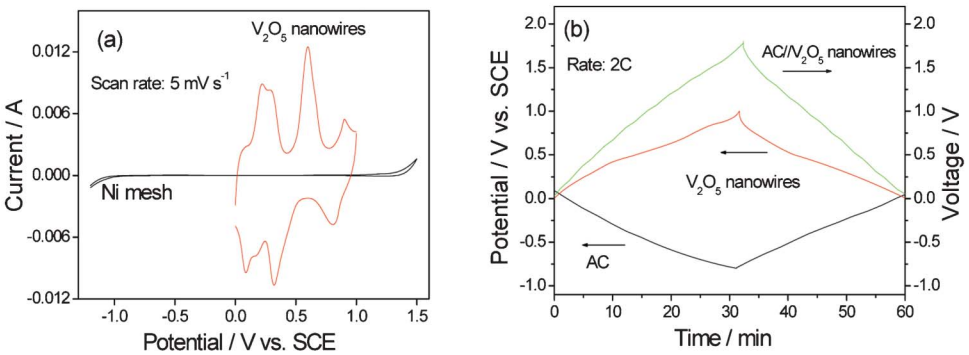

Fig. 12 (a) CV curve of V_2O_5 nanowires and Ni mesh (current collector) and (b) charge/discharge curves of AC//V_2O_5 nanowires in 0.5 mol l^{-1} K_2SO_4 aqueous solution (modified from ref. 6*a*).

 This journal is © The Royal Society of Chemistry 2013

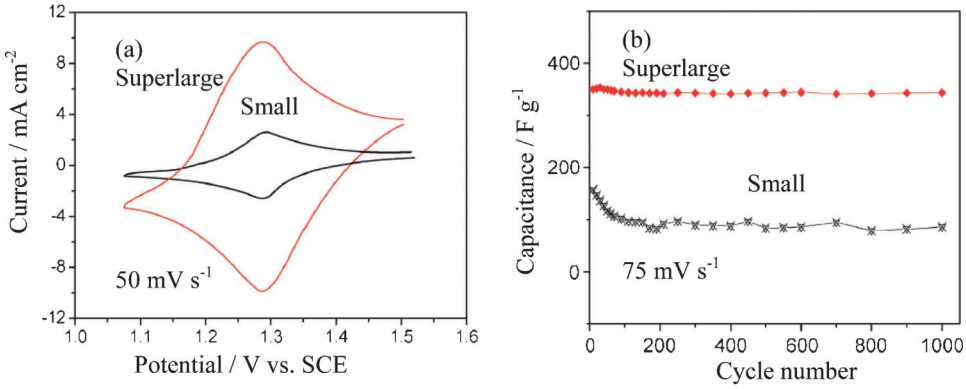

Fig. 13 (a) Typical CV curves and (b) cycling performance of super-large PbO_2 dendrites composed of trigonal nanoplates and the small dendrites in 5.0 mol l^{-1} H_2SO_4 solution recorded a scan rate of 75 mV s^{-1} (modified from ref. 82c).

Published on 16 avril 2013. Downloaded on 2024-08-15 14:15:36.

deposition through templates assembled from submicron diameter PS spheres assembled on either gold or indium tin oxide substrates.[82b] Super-large dendrites (about 500 μm) composed of trigonal PbO_2 nanoplates are synthesized by electrodeposition.[82c] These prepared super-large PbO_2 dendrites composed of orderly arranged trigonal nanoplates.

The CV curve of PbO_2 exhibits one couple of well-defined redox peaks. The potential difference between the oxidation and reduction peaks is usually very large due to the poor kinetics of the PbO_2/Pb^{2+} couple. The thin film PbO_2 on Ti/SnO_2 foil can deliver a discharge specific capacitance of 79.9 F g^{-1} at a current of 0.75 mA cm^{-2} and 74.1 F g^{-1} at 10 mA cm^{-2}, based on the total weight of both active electrode materials, and the capacitance retains 83% of its initial value after 3000 deep cycles at the 4 C rate.[82a] The electrochemical activity of the resulting macroporous β-PbO_2 is greater than that of the corresponding plain film.[82b] The super-large PbO_2 dendrites composed of orderly arranged trigonal nanoplates can promote the remarkable enhancement in the electrochemical performances of the prepared ASCs.[82c] As shown in Fig. 13, the current response and capacitance of the super-large PbO_2 dendrites are much larger than that of the small dendrites in 5.0 mol l^{-1} H_2SO_4 solution.

In the case of the ASCs using PbO_2 as the positive electrode, their performance is dependent on the positive electrode, negative electrode and their ratio. In the voltage range of 0.8–1.8 V, this AC//PbO_2 delivers a specific energy density of 29.0 Wh kg^{-1} at a power density of 1010 W kg^{-1} based on the total weight of both active electrode materials when the value of mass ratio of AC to PbO_2 is three. After 4500 deep cycles at the charge-discharge current of 200 mA g^{-1}, the specific capacitance remains at 64.4 F g^{-1} with the specific energy density of 32.2 Wh kg^{-1} and it only decays 10% of its initial capacity.[8d]

In the ASC based on AC//PbO_2 nanowires, CH_3SO_3H is added to prevent PbO_2 from sulfation. Its energy density can be 29 Wh kg^{-1} at a current density of 10 mA cm^{-2}. There is no sign of degradation during more than 5000 cycles.[9a] For comparison, the AC//PbO_2 thin film system exhibits a 50% decrease of its performances at the similar conditions.

3.2.6 Cobalt oxides. Cobalt oxides mainly refer to Co_3O_4 and $Co(OH)_2$. Strictly speaking, the latter should be ascribed to hydroxides. However, its capacitive behavior is similar to that of Co_3O_4, and it is included in this section. Both of them present a layered structure, and their main reaction mechanisms as a positive electrode material for the ASCs are shown in eqn (18) and (19):

$$Co_3O_4 + H_2O + OH^- \leftrightarrow 3CoOOH + e^- \quad (18)$$

$$3Co(OH)_2 + 2OH^- \leftrightarrow Co_3O_4 + 4H_2O + 2e^- \quad (19)$$

Various methods including solid state syntheses, wet chemical processes, electrodeposition, radio frequency magnetron sputtering and microwave methods can be used to prepare tailored Co_3O_4. To achieve good electrochemical performance, the specific surface area is an important factor. Thin film[83a,83b] and nanostructured Co_3O_4 are preferred.[83c] Co_3O_4 thin films can be deposited directly on current collectors *via* a single step solution precursor plasma spray route. In this approach, an aqueous solution containing cobalt acetate is axially fed into plasma plume to produce nanoparticulates of Co_3O_4 *via* an accelerated thermo-chemical conversion process, which are eventually deposited on a current collector substrate. Thus, Co_3O_4 shows the nano particulate structure with porosity.[83b] Nanostructured Co_3O_4 materials are usually prepared from powders using sol-gel and hydrothermal methods. Utilizing sawdust as a bio-template, Co_3O_4 nanoparticles with the average diameter of about 40 and 60 nm are prepared.[83c]

Co_3O_4 can form composites with conductive materials such as CNTs and graphene. Composites of cobalt oxides/CNTs are prepared by adding and thermally decomposing cobalt nitrates directly onto the surface of CNTs to form cobalt oxides.[84a] A microwave-assisted method can be used to prepare Co_3O_4@graphene nanosheet (GNS) composite with homogeneous distribution of Co_3O_4 nanoparticles (3–5 nm in size) on graphene sheets.[84b] Using a mild hydrothermal method, Co_3O_4 nanoplates with a length of 0.5–1 μm and width of 100–300 nm can be homogeneously distributed on the surface of GNSs.[84c]

As to $Co(OH)_2$, it mainly consists of α- and β-phases. Simple cathodic deposition can achieve films from their chloride

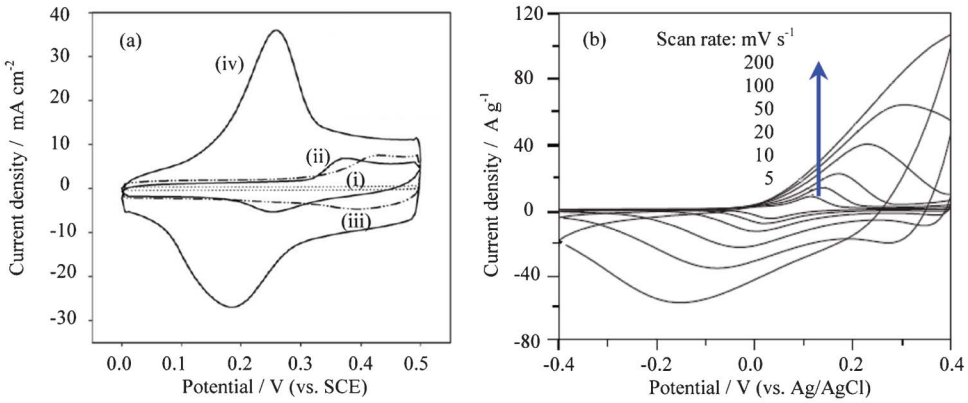

Fig. 14 (a) CV curves of various electrodes at 50 mV s^{-1} in 1 mol l^{-1} KOH solution: (i) CNTs; (ii), nickel oxide/CNTs; (iii) cobalt oxide/CNTs; (iv), nickel-cobalt oxides/CNTs (Ni/Co molar ratio = 1 : 1), and (b) CV curves of α-$Co(OH)_2$ composite electrode recorded in 1 mol l^{-1} KOH aqueous solution at different scan rates (modified from ref. 84*a* and 85c).

Published on 16 avril 2013. Downloaded on 2024-08-15 14:15:36.

precursor in aqueous media.[85a] A highly uniform, porous nanostructured β-$Co(OH)_2$ is synthesized *via* a hydrothermal and template-free approach. The nanostructures consist of amassing, arbitrarily layered, interconnecting nanosheets, resulting in a flower-like structure with many fissures.[85b] Mesoporous α-$Co(OH)_2$ with an average size of 250 nm is synthesized through radiating a cobalt nitrate hexahydrate in the isopropanol solution.[85c]

As eqn (18) showed, Co_3O_4 is mostly used in the ASCs of alkaline solutions though neutral solutions are also used. The electrolyte concentration can affect the specific capacitance and the stability of cobalt oxide film, and the highest specific capacitance of 118 F g^{-1} can be achieved in 1.5 mol l^{-1} KOH at the potential range of −0.4–0.6 V (*vs.* SCE).[83a] The prepared porous Co_3O_4 nanoparticulates show a specific capacitance of about 162 F g^{-1} in 6 mol l^{-1} KOH solution in the potential range of −0.1–0.5 V (*vs.* Ag/AgCl).[83b] In the case of the Co_3O_4 nanoparticles utilizing sawdust as a bio-template can present higher specific capacitance, 290 F g^{-1}, in the same potential range and same KOH solution.[83c]

In the case of the composites of Co_3O_4 with CNTs and graphene, their electrochemical performance is improved. For the composite of cobalt oxide/CNT, a couple of broad redox peaks can be seen at 0.40 and 0.42 V in 1 mol l^{-1} KOH solutions (Fig. 14a), respectively. When nickel oxide is doped, the current response can be more promoted, and a specific capacitance of 569 F g^{-1} at 10 mA cm^{-2} is obtained.[84a] GNSs can effectively restrain the volume expansion of Co_3O_4 nanoplates during cycling and improve the electronic conductivity of the electrode, whereas the Co_3O_4 nanoplates prevent the restacking of the GNSs. As a result, the composite of Co_3O_4 nanoplates with 7.0% GNSs shows a very high specific capacitance of 668 F g^{-1} at 1.25 A g^{-1} in 2 mol l^{-1} KOH solution in the potential range of −0.1–0.5 V (*vs.* SCE).[84c] Furthermore, the composite exhibits a better cycling life.[84b,84c]

For $Co(OH)_2$, its redox potentials are a little lower than those of Co_3O_4. However, its reversibility is very good (Fig. 14b).[85c] $Co(OH)_2$ films (*ca.* 0.4 mg cm^{-2}) show a specific capacitance of 549 F g^{-1}.[85a] Nanostructured $Co(OH)_2$ can be prepared into thin film electrodes *via* screen printing, and their cycling is very good. In 3 mol l^{-1} KOH solution, 99.69% of its maximum capacity can be retained over 600 cycles.[85b] The layer structured mesoporous $Co(OH)_2$ presents a good rate capability. When the scan rate is up to 100 mV s^{-1}, the redox peaks in 1 mol l^{-1} KOH solution can still be clearly identified as shown in Fig. 14b.[85c]

3.3 $Ni(OH)_2$

Nickel hydroxide is a well-known material in the battery field as a positive electrode in nickel-cadmium and nickel-metal hydride batteries.[86a] Its actions in the ASC of AC//$Ni(OH)_2$ is similar to that in the batteries and that of $Co(OH)_2$, which is shown in eqn (20):

$$Ni(OH)_2 + OH^- \leftrightarrow NiOOH + H_2O + e^- \quad (20)$$

The electrolyte is typically KOH aqueous solutions. Like $Co(OH)_2$, its oxide, NiO, can also be used as a positive electrode for ASCs. However, most reports are related to $Ni(OH)_2$. There are three phases for $Ni(OH)_2$: α, β and γ. Alpha-$Ni(OH)_2$ is unstable in alkaline medium but has a higher theoretic capacitance, and transforms to β-$Ni(OH)_2$, which is more stable.[86b] In the case of the γ-$Ni(OH)_2$, it is irreversible and could not be used as an electrode material for batteries and ASCs. As a result, without special explanation, $Ni(OH)_2$ usually means the β phase.

To improve its electrochemical performance, heteroatom doping can be used.[86c,86d,87–89] For example, Co plays an important role in improving electronic conductivity, and Zn, introduced for higher disordering of the $Ni(OH)_2$ lattice, acts to improve the active material utilization and ion-moving path.[88] To increase the specific surface area, nanostructured or porous $Ni(OH)_2$ is preferred.[86d]

Single $Ni(OH)_2$ hexagonal nanoplates can also form composites with AC,[87b,88] CNTs[9b,90a] and GNSs.[90b] The CNTs in the composite can reduce the aggregation of $Ni(OH)_2$ nanoparticles and induce a good distribution of the nanosized $Ni(OH)_2$ particles on the cross-linked, netlike CNT structure.[90a]

The redox behavior of $Ni(OH)_2$ is not very symmetrical, as shown in Fig. 15a.[87b] The specific capacitances of $Ni(OH)_2$ can

 This journal is © The Royal Society of Chemistry 2013

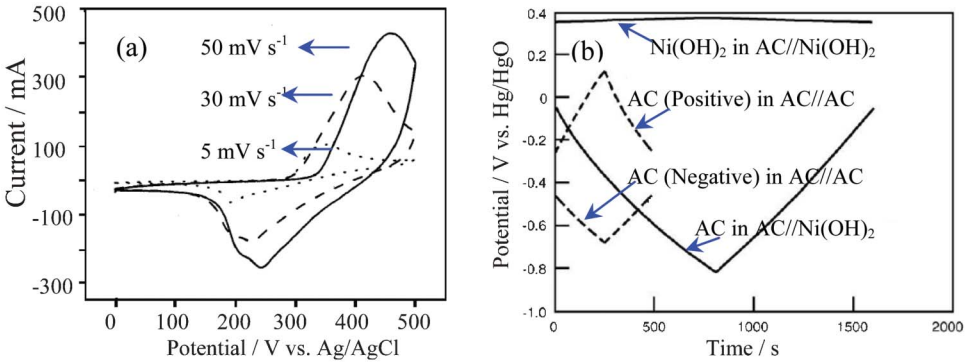

Fig. 15 (a) CV curve of $Ni(OH)_2$ in alkaline solution and (b) charge/discharge curves of the positive and negative electrodes in the AC//$Ni(OH)_2$ ASC and electric double layer capacitors of AC//AC at 1 mA cm^{-2} in 10 mol l^{-1} KOH aqueous solution (modified from ref. 87*b* and 90*c*).

Published on 16 avril 2013. Downloaded on 2024-08-15 14:15:36.

be 2217 F g^{-1}, usually higher than that of $Co(OH)_2$.[85a] When a polymer hydrogel electrolyte from PAAK and 10 mol l^{-1} KOH solution is used instead of liquid solution, the work voltage can be extended and higher capacitance and a better rate capability can be achieved.[90c]

The Co-doped $Ni(OH)_2$ presents a specific capacitances of 684 F g^{-1}, much higher than those of $Ni(OH)_2$ and Co_3O_4 in 1.0 mol l^{-1} NaOH solution in the potential range of −0.05–0.5 V (*vs.* Ag/AgCl), which are about 113 and 161 F g^{-1} at 5 mV s^{-1}, respectively.[86d] The simultaneous presence of Zn and Co ions in the $Ni(OH)_2$ layer improves the efficiency of the active material and reduces the resistance of the unit cell.[86c] The resulting nickel-cobalt hydroxide nanorod arrays on stainless steel achieves a high specific capacitance of 456 F g^{-1} in 1 mol l^{-1} KOH solution.

As for composites of $Ni(OH)_2$ with conductive materials, their rate capability is greatly improved due to good electronic conductivity. In addition, the specific capacitance is also increased. In the case of the $Ni(OH)_2$ composite with AC, the AC can act as an electrolyte reservoir to reduce the ionic diffusion resistance, regardless of the charge/discharge current density. As a result, over 160 F g^{-1} of discharge capacitance can be achieved for $Ni(OH)_2$.[87b] The composite of $Ni(OH)_2$@CNTs can deliver a capacitance of 311 F g^{-1} in 6 mol l^{-1} KOH electrolyte in the potential range of −0.3–0.7 V (*vs.* SCE).[9b] Single $Ni(OH)_2$ hexagonal nanoplates on GNSs also show a high specific capacitance (1335 F g^{-1} at 2.8 A g^{-1}) and remarkable rate capability (953 F g^{-1} at 45.7 A g^{-1}) in 1 mol l^{-1} KOH aqueous electrolyte.[90b]

When $Ni(OH)_2$ and its composites are used as a positive electrode for the ASCs, its energy and power densities are much larger than those of the EDLC. Its typical charge and discharge curves can be shown in Fig. 15b when AC is used as the negative electrode. The ASC from Zn and Co-codoped $Ni(OH)_2$ exhibits a high energy density with 35.7 Wh kg^{-1}, based on the active $Ni(OH)_2$.[86c] The composite of $Ni(OH)_2$ with MWCNT can deliver an energy of 32 Wh kg^{-1} at a specific power of 1500 W kg^{-1} based on the total mass of the active electrode materials. It also exhibits good cycling performance and 90% of its initial capacity is retained for over 2000 cycles.[90a]

In the case of the α-$Ni(OH)_2$, it can be stabilized by doping. For example, when 7.5% Al is doped, the Al-doped α-$Ni(OH)_2$ materials delivers a high specific capacitance (2.08×10^3 F g^{-1}) and excellent rate capability.[86b] Of course, further work is needed for its possible application.

3.4 Intercalation compounds

Intercalation compounds have attracted a lot of interest thanks to their large specific charge. They have been typically used in organic electrolytes but aqueous examples are more interesting.

3.4.1 $LiCoO_2$. $LiCoO_2$ is a hexagonal layered structure belonging to *Pnm* space group with a = 0.2816 nm and c = 1.4056 nm. It is widely applied in lithium ion batteries due to its stable structure during charging and discharging. Due to the good reversibility of intercalation/de-intercalation of Li^+ ions, which is shown in eqn (21), it could be used as positive electrode for aqueous ASCs.[91a]

$$LiCoO_2 \leftrightarrow Li_{1-x}CoO_2 + xLi^+ + xe^- \ (x \leqslant 0.5) \qquad (21)$$

Its traditional preparation method is *via* solid-state reaction. In order to get better electrochemical performance, nano structured $LiCoO_2$ has been prepared by sol-gel methods for application in ASCs.[5a,42b,9c]

CV curves (Fig. 16) of $LiCoO_2$ in a saturated aqueous Li_2SO_4 solution show that the intercalation and de-intercalation of lithium ions are similar to organic electrolyte solutions.[92] There are also three couples of redox peaks for $LiCoO_2$ in the aqueous solution, located at 0.87/0.71, 0.95/0.90 and 1.06/1.01 V (*vs.* SCE), which agree well with those in the organic electrolyte solution at 4.08/3.83, 4.13/4.03 and 4.21/4.14 V (*vs.* Li/Li^+). The evolution of oxygen (about 1.7 V *vs.* SCE) in the aqueous electrolyte occurs at much higher potential, indicating the good electrochemical stability of $LiCoO_2$ as the positive electrode of the ASCs. The diffusion coefficient of the lithium ions is of the same magnitude as that in the organic electrolyte; however, the current response and reversibility of redox behavior in the aqueous solution are better than those in the organic electrolytes due to its higher ionic conductivity.[93,94]

Published on 16 avril 2013. Downloaded on 2024-08-15 14:15:36.

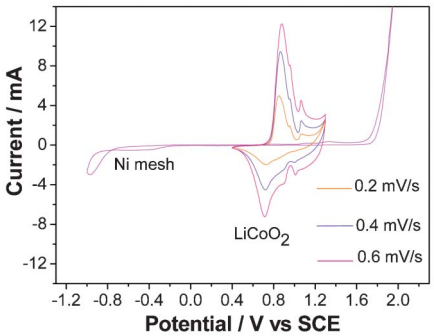

Fig. 16 CV curves of $LiCoO_2$ and nickel mesh in saturated Li_2SO_4 solution (modified from ref. 92).

AC//nano-$LiCoO_2$ in 0.5 mol l^{-1} Li_2SO_4 solution at 1 A g^{-1} between 0–1.8 V shows high capacitance and efficiency. The efficiency of this system increases to nearly 100% after the initial cycle and the capacity does not change much after 40 cycles.[94b]

Due to the high cost of cobalt, there is not much work on its redox behavior in aqueous solutions.

3.4.2 $LiMn_2O_4$. $LiMn_2O_4$, whose reaction mechanism is shown in eqn (22) and is similar to that of $LiCoO_2$, is found to be a good positive electrode for aqueous ASCs due to its low cost compared to $LiCoO_2$.[95] It mainly exists in a spinel structure. Manganese cations occupy half of the octahedral interstitial sites and Li^+ ions occupy one eighth of tetrahedral sites. The Mn_2O_4 framework provides 3D interstitial space for Li^+ ion transport, maintaining its structure over the compositional range Li_xMnO_4 ($0 < x < 1$) by changing the average Mn oxidation state between 3.5 and 4.0.[96] As early as 1994, it was reported for the first time that $LiMn_2O_4$ can de-intercalate and intercalate Li^+ ions in aqueous electrolyte.[97,98]

$$LiMn_2O_4 \leftrightarrow Li_{1-x}Mn_2O_4 + xLi^+ + xe^- \ (x \leqslant 1) \qquad (22)$$

The $LiMn_2O_4$ spinel can be prepared by solid-state reaction, sol-gel method and hydrothermal methods.[5a,42b] Among them, one-dimensional (1D) nanostructures including nanowires, nanotubes and nanorods have attracted special attention.[9d,10b,99] Porous $LiMn_2O_4$ can be prepared by template methods. For example, when PS particles from emulsion polymerization are used as a template, a porous $LiMn_2O_4$ consisting of nanograins is conveniently prepared, whose morphology is shown in Fig. 17a.[10b] To improve the structural stability of $LiMn_2O_4$ from solid-state reaction, it can also be doped by heteroatoms such as Al, Cr, Cr–Fe and Ni like in organic electrolytes.[100–103]

In the CV curve of $LiMn_2O_4$ in the saturated Li_2SO_4 solution, as shown in Fig. 17b, there are two evident couples of redox peaks at 0.85/0.69 V and 0.98/0.82 V (V *vs.* SCE), respectively. This agrees well with the de-intercalation and intercalation reactions of Li^+ ions in organic electrolytes, which also show two couples of redox peaks. They are also much lower than the potential for oxygen evolution (about 1.7 V *vs.* SCE) indicating the good stability of $LiMn_2O_4$ as the positive electrode for the ASCs in aqueous solutions.[104]

In the case of porous or nanostructured materials as electrode materials for electrochemical energy storage systems, they have shown some advantages such as higher capacities and better rate capability over traditional micrometer-sized materials.[9d,10a,10b,105a] For example, $LiMn_2O_4$ nanochains exhibit a high reversible capacity of 110 mAh g^{-1} at 4.5 C and 95 mAh g^{-1} even at 91 C in 0.5 mol l^{-1} Li_2SO_4 aqueous electrolyte. When charged at 136 C, 84% capacity could be obtained.[10a]

The ASC using micrometer $LiMn_2O_4$ as the positive electrode and AC as the negative electrode in a 1 mol l^{-1} Li_2SO_4 solution, the specific energy can be 38 Wh kg^{-1} at a power density of 100 W kg^{-1}, and still keeps 23 Wh kg^{-1} at a power density of 760 W kg^{-1} based on the total weight of the active materials of both electrodes.[5a] In the case of the nanostructured $LiMn_2O_4$, when they are assembled into ASCs, power density and cycling behavior are greatly improved. For example, the ASC of AC//$LiMn_2O_4$ nanorod presents very high power density in 0.5 mol l^{-1} Li_2SO_4, up to 14.5 kW kg^{-1}, and there is still 94% capacity retention after 1200 full cycles.[9d,99] The ASC of AC//porous $LiMn_2O_4$ in 0.5 mol l^{-1} Li_2SO_4 aqueous solution show excellent cycling performance at the rate of 9C (1000 mA g^{-1}), with no more than 7% capacity loss after 10 000 cycles.[10b] The cycling behavior of AC//porous $LiMn_2O_4$ is the best amongst the reported $LiMn_2O_4$. The nanograins in the porous $LiMn_2O_4$ could restrain the Mn^{3+} on the surface from dissolution, which can also accommodate effectively the

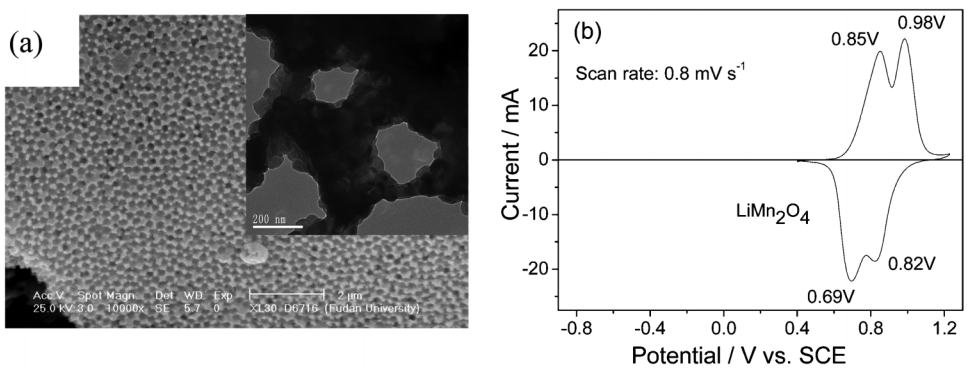

Fig. 17 (a) SEM micrograph of the porous $LiMn_2O_4$ and (b) CV curve of the micrometer $LiMn_2O_4$ in the saturated Li_2SO_4 solution (modified from ref. 10*b* and 104).

 This journal is © The Royal Society of Chemistry 2013

Published on 16 avril 2013. Downloaded on 2024-08-15 14:15:36.

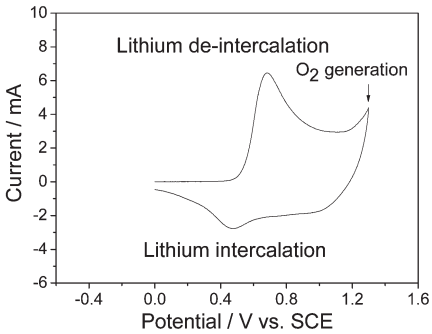

Fig. 18 CV curve of in $LiNi_{1/3}Co_{1/3}Mn_{1/3}O_2$ in 2 mol l^{-1} Li_2SO_4 aqueous solution (modified from ref. 108).

strain caused by Jahn–Teller distortion during the charge and discharge process and favor the morphological and structural stability.[10b]

Doping the micrometer-sized $LiMn_2O_4$ with several cations is also a good way to effectively reduce the Jahn–Teller distortion and further improve the cycling stability.[105] In the CV curve of $LiCr_{0.15}Mn_{1.85}O_4$ in the saturated aqueous $LiNO_3$ (9 mol l^{-1}) solution, faster "CV response" of $LiCr_{0.15}Mn_{1.85}O_4$ is in correlation with higher capacity retention in comparison to undoped $LiMn_2O_4$.[100] The Ni-doped $LiMn_2O_4$ presents much better rate capability and cycling behavior.[103]

3.4.3 $Li[NiCoMn]_{1/3}O_2$. $LiNi_{1/3}Co_{1/3}Mn_{1/3}O_2$ has a rhombohedral structure belonging to the *R*3*m* space group of a hexagonal α-$NaFeO_2$ structure. The lattice is formed by oxygen atoms in ABC stacking with alternating layers containing mixtures of nickel (+2), cobalt (+3), and manganese (+4) atoms. Its reaction mechanism as a positive electrode for ASCs is as shown in eqn (23). During the de-intercalation of Li^+ ions, the valence of Ni is changed from +2 to +3, and that of Co from +3 to +4. In the meanwhile, Mn stays at +4. $LiNi_{1/3}Co_{1/3}Mn_{1/3}O_2$ powders are traditionally synthesized from heat-treating the coprecipitated spherical metal hydroxide with lithium salt or hydroxide.[106]

$$\begin{aligned} &Li[Ni(II)]_{1/3}[Co(III)]_{1/3}[Mn(IV)]_{1/3}O_2 \leftrightarrow \\ &Li_{1-x}Li[Ni(III)]_{1/3}[Co(IV)]_{1/3}[Mn(IV)]_{1/3}O_2 + xLi^+ + xe^- \end{aligned} \quad (23)$$

The electrochemical stability of $LiNi_{1/3}Co_{1/3}Mn_{1/3}O_2$ in a Li^+-containing aqueous solution is critically dependent on the pH value.[107] As shown in Fig. 18, one couple of its redox peaks in 2 mol l^{-1} Li_2SO_4 solution are situated at 0.48 and 0.68 V (*vs.* SCE), corresponding to the intercalation and de-intercalation of lithium ions in $LiNi_{1/3}Co_{1/3}Mn_{1/3}O_2$, respectively. The oxygen evolution potential shifts to 1.29 V (*vs.* SCE), which is much lower than those for $LiCoO_2$ and $LiMn_2O_4$ systems. It shows that it is possible to extract lithium ions from the host before the evolution of oxygen.[108] However, the CV response and symmetry of the redox peaks are not good.

The cycling performance of $LiNi_{1/3}Co_{1/3}Mn_{1/3}O_2$ is not good, which can not be comparable with that of $LiCoO_2$ or $LiMn_2O_4$.[93,105c] It was believed that the proton intercalation occurred in parallel with Li^+ intercalation when the $LiNi_{1/3}Co_{1/3}Mn_{1/3}O_2$ electrode was discharged in neutral solution, which led to serious capacity fading. However, there is no direct evidence. If this is true, then the cycling of $LiCoO_2$ and $LiMn_2O_4$ should also be poor, which contradicts the experimental results. In addition, it is curious that $LiNi_{1/3}Co_{1/3}Mn_{1/3}O_2$ synthesized by the sol-gel method can exhibit a good cycling performance in a 2 mol l^{-1} $LiNO_3$ aqueous solution at different charge/discharge rates from 80 to 200 C in spite of low capacity.[109] As a result, further research are needed.

The electrochemical performance of $LiNi_{1/3}Mn_{1/3}Co_{1/3}O_2$ in aqueous solution can be modified by mixing with PPy.[110] The redox reversibility and capacity retention are much improved compared to those of the pristine $LiNi_{1/3}Mn_{1/3}Co_{1/3}O_2$. The main reason is that the added PPy could enhance the electronic conductivity of $LiNi_{1/3}Mn_{1/3}Co_{1/3}O_2$ electrode.

3.4.4 Other intercalation compounds. Beside lithium intercalation compounds, other intercalation compounds such as sodium and potassium can also be used as positive electrodes such as $NaMnO_2$[10c], $Na_{0.6}CoO_2$[111a] and $KMnO_2$[10d]. Since the sizes of Na^+ and K^+ are larger than that of Li^+, their structure is not $LiMn_2O_4$ spinel but instead layered $LiMnO_2$. Both of them can be prepared by solid-state reaction.

In the CV curve of $NaMnO_2$ (Fig. 19a), its shape slightly deviates from the ideal rectangular with two small redox couples, indicative of the pseudocapacitance properties, which are ascribed to the intercalation/de-intercalation of Na^+ into and from the solid lattice.[10c] As for $KMnO_2$ (Fig. 19a), it was found for the first time to present a sharp redox couple at 0.35 and 0.60 V (*vs.* SCE), which are owned to the intercalation/de-intercalation of K^+ into and from the solid lattice.[10d] Their supercapacitive behaviors can also be observed from their charge and discharge curves in Fig. 19b and Fig. 19c.

The AC//$NaMnO_2$ and AC//$KMnO_2$ ASCs exhibit sloping voltage–time curves in the entire voltage region of 0 to 1.9 V (Fig. 19b and Fig. 19c). They deliver energy densities of 19.5 Wh kg^{-1} and 25.3 Wh kg^{-1}, respectively, based on the total mass of the active electrode materials and excellent cycling behavior without removal of oxygen in the electrolytes. For example, in the case of AC//$KMnO_2$ ASC, after 10 000 full cycles there is no evident capacity fading and the Coulomb efficiency is 100% (Fig. 19d). The latter shows better rate behavior, with an energy density of 17.6 Wh kg^{-1} at a power density of 2 kW kg^{-1}.[10d] These ASCs are promising for practical applications because of its low price, easy preparation and excellent cycling behavior.

3.5 Other positive materials

Conductive polymers such as PAn, PPy and polythiophene, which can be p-doped, can also be positive electrodes for ASCs. Their electrochemical performance can be improved by nanostructuring, adding metal oxides such as SnO_2, Fe_3O_4 and TiO_2 and conductive materials such as MWCNT.[111b] Some book chapters[5a] and reviews[16b,16c,16d] can be referred, and they will not be expounded here.

4. Summary and perspective

In summary, it is clear that the above mentioned electrode materials can build up ASCs of higher energy and power

Published on 16 avril 2013. Downloaded on 2024-08-15 14:15:36.

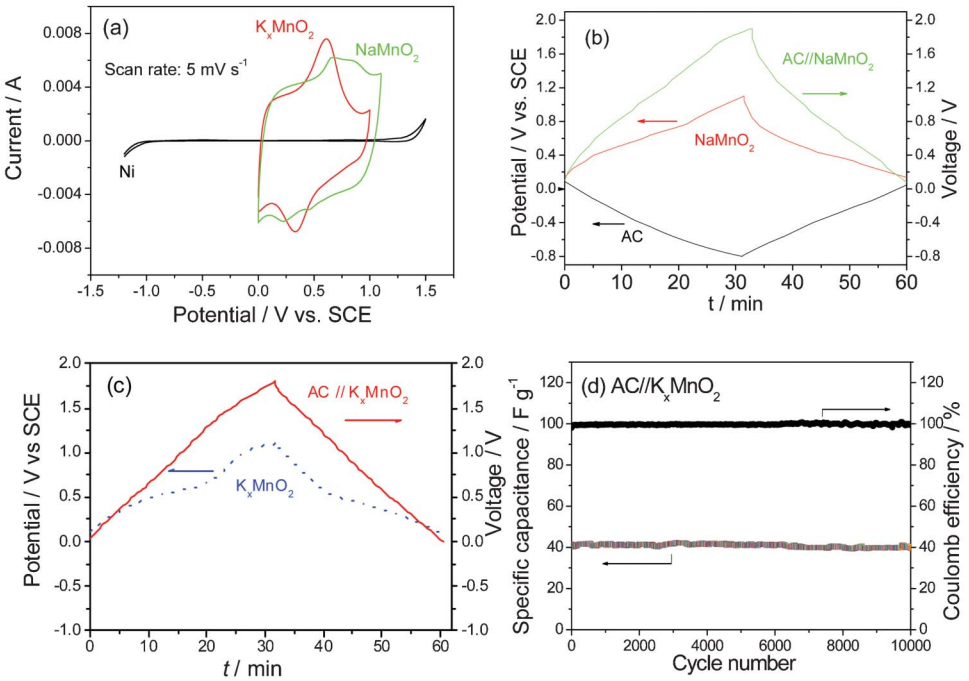

Fig. 19 (a) CV curves of $NaMnO_2$ and K_xMnO_2 in 0.5 mol l^{-1} Na_2SO_4 and K_2SO_4 aqueous solution, charge and discharge curves of (b) AC//AC, $NaMnO_2$ and AC//$NaMnO_2$ hybrid superapacitors in 0.5 mol l^{-1} Na_2SO_4 aqueous solution, (c) K_xMnO_2 and AC//K_xMnO_2 hybrid supercapacitors in 0.5 mol l^{-1} K_2SO_4 aqueous solution, and (d) cycling behavior of the AC//K_xMnO_2 ASC (modified from ref. 10*c* and 10*d*).

densities in comparison with the traditional EDLCs. For example, the intercalation compounds present some evident advantages over other positive electrodes. The shuttled cations exist originally in the intercalation compounds. During the charge and discharge process, the concentrations of aqueous electrolytes do not change and the ionic conductivities of the electrolytes keep stable. As a result, not only the electrochemical performance can be kept stable during charge and discharge process, but also the amount of electrolytes will be much less than those required for the traditional EDLCs and the other ASCs, leading to higher energy and power densities. To further increase the power density of the ASCs, adding conductive agents, increasing surface area and nano structuring have achieved great advances. To improve their cycling performance, surface modification is an efficient method.

The realization of high-efficiency energy storage is one of the greatest scientific and engineering challenges at present, so the design of novel ASCs is an interesting ongoing development and the continued and ever-lasting study is expected. The promising strategies for the further development of advanced electrode materials for ASCs in aqueous electrolytes are generalized as the following:

Both surface and bulk (crystal structure and microstructure) are actively involved in the charge storage process. Designing superior architectures with high surface area and special structure (such as 3D or hierarchical nanostructures, mesoporous, synergetic core-shell structures and ordered nanostructure arrays) are a possible route to maximize the electrochemically active sites for redox reactions or chemical absorption/desorption and to further increase the energy storage density.[60a,112a]

It is important to investigate the physical/chemical properties of the interface within the ASC structure as well as their effects on the electrochemical performance.[114a] Challenges remain for understanding the fade mechanisms of various electrodes in aqueous electrolytes. Moreover, theoretical and computational modeling and simulation are also effective in predicting the properties and optimizing the composition of electrode materials used in energy storage systems.[2b,114b] The combination of theoretical calculations and experimental investigations will promote the exploration of novel high-performance energy storage materials.

It is well understood that by using nanostructured materials, the ion diffusion length is reduced and the inner stress can be alleviated, and thus better rate capability and cyclability can be expected. Electrode materials with mesoporous structures can accommodate large volume changes during the charge/discharge process, and the hollow structures may provide extra space for ion storage.[6,112b] Hierarchical nanostructures, combining microscale and nanoscale materials, may capitalize on the advantages and restrain the shortcomings of the two components.[112c,d] Besides, nanostructured current collectors and flexible paper/textile electrodes will gain attention in the future.[112e,f] Nanostructured current collectors, which have much larger surface areas and good mechanical robustness, can provide both efficient pathways for ion and electron transport through the entire electrode architecture.

 This journal is © The Royal Society of Chemistry 2013

Published on 16 avril 2013. Downloaded on 2024-08-15 14:15:36.

There is still some development before the practical applications of ASCs in terms of cycling stabilities. Therefore, it is urgent to improve their overall performance, which depends not only on advanced positive materials but also negative materials.[6c,111c] The development of new high-performance negative electrode materials is more imminent.

Aqueous electrolytes show promising progress to address the energy challenge for future clean and sustainable energy source. However, the electrolytes for some ASCs are strong acid or alkali,[113] which are not environmentally friendly compared to neutral aqueous electrolytes. Electrode materials with high energy density and power density in neutral aqueous electrolytes are desirable. In addition, an appropriate amount of organic additives should be determined because the oxide film may form a few layers of oxide film during the charge and discharge process, which would relieve capacity fading, especially for metal oxides and intercalation compounds.

While tremendous work has been made in the syntheses of various composites for ASCs, a better understanding of how synthesis techniques, composition, and morphology affect the electrochemical performance is also important.[115] For some future applications, the development of simple, new and efficient synthesis and fabrication processes are necessary to further improve the practicality of aqueous ASCs towards commercialization. The materials (such as Na_xMnO_2[10c] and K_xMnO_2[10d]) prepared by a simple method with low costs have comparable advantages in commercial capacitors.

Acknowledgements

Financial support from MOST (2010DFA61770), STCSM (12JC1401200) and NSFC (21 073 046) is greatly appreciated.

References

1 (*a*) H. Nishide and K. Oyaizu, *Science*, 2008, **319**, 737; (*b*) J. M. Tarascon and M. Armand, *Nature*, 2001, **414**, 359; (*c*) J. A. Rogers, T. Someya and Y. G. Huang, *Science*, 2010, **327**, 1603; (*d*) F. Meng and Y. Ding, *Adv. Mater.*, 2011, **23**, 4098; (*e*) P. Simon and Y. Gogotsi, *Nat. Mater.*, 2008, **7**, 845.

2 (*a*) B. E. Conway, *Electrochemical Supercapacitors: Scientific Fundamentals and Technological Applications*, Plenum Publishers, New York, 1999; (*b*) S. N. Razumov, A. Klementov, S. Litvinenko and A. Beliakov, *U. S. Patent* No. 6,222,723 (2001); (*c*) D. Cericola and R. Kötz, *Electrochim. Acta*, 2012, **72**, 1; (*d*) M. S. Hong, S. H. Lee and S. W. Kim, *Electrochem. Solid-State Lett.*, 2002, **5**, A227.

3 H. Nishihara and T. Kyotani, *Adv. Mater.*, 2012, **24**, 4473.

4 (*a*) W. Li, W. R. McKinnon and J. R. Dahn, *J. Electrochem. Soc.*, 1994, **141**, 2310; (*b*) Q. Wang, Z. Wen and J. Li, *Adv. Funct. Mater.*, 2006, **16**, 2141; (*c*) H. J. Liu, W. J. Cui, L. H. Jin, C. X. Wang and Y. Y. Xia, *J. Mater. Chem.*, 2009, **19**, 3661; (*d*) R. Ruffo, F. L. Mantia, C. Wessells, R. A. Huggins and Y. Cui, *Solid State Ionics*, 2011, **192**, 289; (*e*) H. Manjunatha, G. S. Suresh and T. V. Venkatesha, *J. Solid State Electrochem.*, 2011, **15**, 431.

5 (*a*) Z. B. Wen, S. Tian, L. L. Liu and Y. P. Wu, Chapter 13 Controlled particle size and shape of nanomaterials and their applications in supercapacitors, in *Controlled Size and Shape of Nanostructured Materials and Their Applications*, pp. 473–519, Pan Stanford Publishing Pte Ltd, Singapore, 2012; (*b*) K. Xie, X. T. Qin, X. Z. Wang, Y. N. Wang, H. S. Tao, Q. Wu, L. J. Yang and Z. Hu, *Adv. Mater.*, 2012, **24**, 347; (*c*) L. L. Zhang and X. S. Zhao, *Chem. Soc. Rev.*, 2009, **38**, 2520; (*d*) Y. Zhai, Y. Dou, D. Zhao, P. F. Fulvio, R. T. Mayes and S. Dai, *Adv. Mater.*, 2011, **23**, 4828.

6 (*a*) Q. T. Qu, Y. Shi, L. L. Li, W. L. Guo, Y. P. Wu, H. P. Zhang, S. Y. Guan and R. Holze, *Electrochem. Commun.*, 2009, **11**, 1325; (*b*) Q. T. Qu, Y. S. Zhu, X. W. Gao and Y. P. Wu, *Adv. Energy Mater.*, 2012, **2**, 950; (*c*) W. Tang, L. Liu, S. Tian, L. Li, Y. Yue, Y. P. Wu and K. Zhu, *Chem. Commun.*, 2011, **47**, 10058; (*d*) Y. G. Wang, Z. D. Wang and Y. Y. Xia, *Electrochim. Acta*, 2005, **50**, 5641; (*e*) M. C. Liu, L. Bin Kong, C. Lu, X. M. Li, Y. C. Luo and L. Kang, *RSC Adv.*, 2012, **2**, 1890; (*f*) Z. Chen, D. Weng, H. Sohn, M. Cai and Y. Lu, *RSC Adv.*, 2012, **2**, 1755.

7 (*a*) T. Brousse, P. L. Taberna, O. Crosnier, R. Dugas, P. Guillemet, Y. Scudeller, Y. Zhou, F. Favier, D. Belanger and P. Simon, *J. Power Sources*, 2007, **173**, 633; (*b*) Y. T. Wang, A. H. Lu and W. C. Li, *Microporous Mesoporous Mater.*, 2012, **153**, 247; (*c*) Q. T. Qu, P. Zhang, B. Wang, Y. H Chen, S. Tian, Y. P. Wu and R. Holze, *J. Phys. Chem. C*, 2009, **113**, 14020; (*d*) W. Tang, Y. Y. Hou, X. J. Wang, Y. Bai, Y. S. Zhu, H. Sun, Y. B. Yue, Y. P. Wu, K. Zhu and R. Holze, *J. Power Sources*, 2012, **197**, 330.

8 (*a*) G. Yu, L. Hu, M. Vosgueritchian, H. Wang, X. Xie, J. R. McDonough, X. Cui, Y. Cui and Z. Bao, *Nano Lett.*, 2011, **11**, 2905; (*b*) Z. Fan, J. Yan, T. Wei, L. Zhi, G. Ning, T. Li and F. Wei, *Adv. Funct. Mater.*, 2011, **21**, 2366; (*c*) Z. S. Wu, W. Ren, D. W. Wang, F. Li, B. Liu and H. M. Cheng, *ACS Nano*, 2010, **4**, 5835; (*d*) N. Yu and L. Gao, *Electrochem. Commun.*, 2009, **11**, 220.

9 (*a*) P. Perret, Z. Khani, T. Brousse, D. Bélanger and D. Guay, *Electrochim. Acta*, 2011, **56**, 8122; (*b*) X. F. Wang, D. B. Ruan and Z. Yu, *Trans. Nonferrous Met. Soc. China*, 2006, **16**, 1129; (*c*) W. Tang, L. L. Liu, S. Tian, L. Li, Y. B. Yue, Y. P. Wu, S. Y. Guan and K. Zhu, *Electrochem. Commun.*, 2010, **12**, 1524; (*d*) W. Tang, L. L. Li, S. Tian, L. Li, L. L. Li, Y. B. Yue, Y. Bai, Y. P. Wu, K. Zhu and R. Holze, *Electrochem. Commun.*, 2011, **13**, 1159.

10 (*a*) W. Tang, S. Tian, L. L. Liu, L. Li, H. P. Zhang, Y. B. Yue, Y. Bai, Y. P. Wu and K. Zhu, *Electrochem. Commun.*, 2011, **13**, 205; (*b*) Q. T. Qu, L. J. Fu, X. Y. Zhan, D. Samuelis, J. Maier, L. Li, S. Tian, Z. H. Li and Y. P. Wu, *Energy Environ. Sci.*, 2011, **4**, 3985; (*c*) Q. T. Qu, Y. Shi, S. Tian, Y. H. Chen, Y. P. Wu and R. Holze, *J. Power Sources*, 2009, **194**, 1222; (*d*) Q. T. Qu, L. Li, S. Tian, W. Guo, Y. P. Wu and R. Holze, *J. Power Sources*, 2010, **195**, 2789.

11 (*a*) M. M. Titirici and M. Antonietti, *Chem. Soc. Rev.*, 2010, **39**, 103; (*b*) M. Endo, Y. J. Kim, H. Ohta, K. Ishii, T. Inoue, T. Hayashi, Y. Nishimura, T. Maeda and M. S. Dresselhaus, *Carbon*, 2002, **40**, 2613; (*c*) D. L. Castello, D. C. Amoros, A. L. Solano, S. Shiraishi, H. Kurihara and A. Oya, *Carbon*, 2003, **41**, 1765.

Published on 16 avril 2013. Downloaded on 2024-08-15 14:15:36.

12 (*a*) D. Qu, *J. Power Sources*, 2002, **109**, 403; (*b*) E. Raymundo-Pinero, K. Kierzek, J. Machnikowski and F. Beguin, *Carbon*, 2006, **44**, 2498.
13 Q. T. Qu, B. Wang, L. C. Yang, Y. Shi, S. Tian and Y. P. Wu, *Electrochem. Commun.*, 2008, **10**, 1652.
14 (*a*) R. N. Reddy and R. G. Reddy, *J. Power Sources*, 2003, **124**, 330; (*b*) H. Inoue, T. Morimoto and S. Nohara, *Electrochem. Solid-State Lett.*, 2007, **10**, A261.
15 (*a*) R. H. Baughman, A. A. Zakhidov and W. A. D. Heer, *Science*, 2002, **297**, 787; (*b*) C. Du and N. Pan, *J. Power Sources*, 2006, **160**, 1487.
16 (*a*) Y. P. Wu, E. Rahm and R. Holze, *J. Power Sources*, 2003, **114**, 228; (*b*) G. P. Wang, L. Zhang and J. J. Zhang, *Chem. Soc. Rev.*, 2012, **41**, 797; (*c*) G. A. Snook, P. Kao and A. S. Best, *J. Power Sources*, 2011, **196**, 1; (*d*) H. Pan, J. Y. Li and Y. P. Feng, *Nanoscale Res. Lett.*, 2010, **5**, 654; (*e*) Y. P. Wu, E. Rahm and R. Holze, *Electrochim. Acta*, 2002, **47**, 3491.
17 (*a*) T. Chen, Z. Cai, Z. Yang, L. Li, X. Sun, T. Huang, A. Yu, H. G. Kia and H. Peng, *Adv. Mater.*, 2011, **23**, 4620; (*b*) Y. Fang, F. Jiang, H. Liu, X. Wu and Y. Lu, *RSC Adv.*, 2012, **2**, 6562; (*c*) E. Frackowiak and F. Beguin, *Carbon*, 2002, **40**, 1775.
18 (*a*) C. G. Liu, M. Liu, F. Li and H. M. Cheng, *Appl. Phys. Lett.*, 2008, **92**, 143108; (*b*) K. H. An, W. S. Kim, Y. S. Park, J. M. Moon, D. J. Bae, S. C. Lim, Y. S. Lee and Y. H. Lee, *Adv. Funct. Mater.*, 2001, **11**, 387.
19 Y. Huang, J. Liang and Y. Chen, *Small*, 2012, **8**, 1805.
20 K. S. Novoselov, A. K. Geim, S. V. Morozov, D. Jiang, Y. Zhang, S. V. Dubonos, I. V. Grigorieva and A. A. Firsov, *Science*, 2004, **306**, 666.
21 C. N. R. Rao, A. K. Sood, K. S. Subrahmanyam and A. Govindaraj, *Angew. Chem., Int. Ed.*, 2009, **48**, 7752.
22 (*a*) Y. Sun, Q. Wu and G. Shi, *Energy Environ. Sci.*, 2011, **4**, 1113; (*b*) D. A. C. Brownson, D. K. Kampouris and C. E. Banks, *J. Power Sources*, 2011, **196**, 4873; (*c*) S. Bai and X. Shen, *RSC Adv.*, 2012, **2**, 64.
23 (*a*) Y. Hernandez, V. Nicolosi, M. Lotya, F. M. Blighe, Z. Y. Sun, S. De, I. T. McGovern, B. Holland, M. Byrne, Y. K. Gunko, J. bJ. Boland, P. Niraj, G. Duesberg, S. Krishnamurthy, R. Goodhue, J. Hutchison, V. Scardaci, A. C. Ferrari and J. N. Coleman, *Nat. Nanotechnol.*, 2008, **3**, 563; (*b*) C. E. Hamilton, J. R. Lomeda, Z. Z. Sun, J. M. Tour and A. R. Barron, *Nano Lett.*, 2009, **9**, 3460.
24 S. Park and R. S. Ruoff, *Nat. Nanotechnol.*, 2009, **4**, 217.
25 D. A. Dikin, S. Stankovich, E. J. Zimney, R. D. Piner, G. H. B. Dommett, G. Evmenenko, S. T. Nguyen and R. S. Ruoff, *Nature*, 2007, **448**, 457.
26 (*a*) D. Li, M. B. Muller, S. Gilje, R. B. Kaner and G. G. Wallace, *Nat. Nanotechnol.*, 2008, **3**, 101; (*b*) M. Lotya, Y. Hernandez, P. J. King, R. J. Smith, V. Nicolosi, L. S. Karlsson, F. M. Blighe, S. De, Z. M. Wang, I. T. M. Govern, G. S. Duesberg and J. N. Coleman, *J. Am. Chem. Soc.*, 2009, **131**, 3611; (*c*) S. Stankovich, D. A. Dikin, R. D. Piner, K. A. Kohlhaas, A. Kleinhammes, Y. Jia, Y. Wu, S. T. Nguyen and R. S. Ruoff, *Carbon*, 2007, **45**, 1558; (*d*) H. L. Guo, X. F. Wang, Q. Y. Qian, F. B. Wang and X. H. Xia, *ACS Nano*, 2009, **3**, 2653.
27 A. K. Geim and K. S. Novoselov, *Nat. Mater.*, 2007, **6**, 183.
28 T. Kuila, S. Bose, A. K. Mishra, P. Khanra, N. H. Kim and J. H. Lee, *Prog. Mater. Sci.*, 2012, **57**, 1061.
29 X. Zhao, L. Zhang, S. Murali, M. D. Stoller, Q. Zhang, Y. Zhu and R. S. Ruoff, *ACS Nano*, 2012, **6**, 5404.
30 L. Zhang and G. Q. Shi, *J. Phys. Chem. C*, 2011, **115**, 17206.
31 D. R. Rolison, J. W. Long, J. C. Lytle, A. E. Fischer, C. P. Rhodes, T. M. McEvoy, M. E. Bourg and A. M. Lubers, *Chem. Soc. Rev.*, 2009, **38**, 226.
32 (*a*) B. G. Choi, M. H. Yang, W. H. Hong, J. W. Choi and Y. S. Huh, *ACS Nano*, 2012, **6**, 4020; (*b*) G. Q. Ning, Z. J. Fan, G. Wang, J. S. Gao, W. Z. Qian and F. Wei, *Chem. Commun.*, 2011, **47**, 5976.
33 S. H. Lee, H. W. Kim, J. O. Hwang, W. J. Lee, J. Kwon, C. W. Bielawski, R. S. Ruoff and S. O. Kim, *Angew. Chem., Int. Ed.*, 2010, **49**, 10084.
34 X. Lu, H. Dou, B. Gao, C. Yuan, S. Yang, L. Hao, L. Shen and X. Zhang, *Electrochim. Acta*, 2011, **56**, 5115.
35 (*a*) S. Stankovich, D. A. Dikin, G. H. B. Dommett, K. M. Kohlhaas, E. J. Zimney, E. A. Stach, R. D. Piner, S. T. Nguyen and R. S. Ruoff, *Nature*, 2006, **442**, 282; (*b*) J. Liu, J. An, Y. Zhou, Y. Ma, M. Li, M. Yu and S. Li, *ACS Appl. Mater. Interfaces*, 2012, **4**, 2870; (*c*) Q. Wu, Y. I. Xu, Z. Yao, A. Liu and G. Shi, *ACS Nano*, 2010, **4**, 1963; (*d*) N. A. Kumar, H. J. Choi, Y. R. Shin, D. W. Chang, L. Dai and J. B. Baek, *ACS Nano*, 2012, **6**, 1715; (*e*) P. Si, S. Ding, X. W. Lou and D. H. Kim, *RSC Adv.*, 2011, **1**, 1271; (*f*) S. H. Aboutalebi, A. T. Chidembo, M. Salari, K. Konstantinov, D. Wexler, H. K. Liu and S. X. Dou, *Energy Environ. Sci.*, 2011, **4**, 1855.
36 Z. Liu, S. W. Tay and X. Li, *Chem. Commun.*, 2011, **47**, 12473.
37 M. Sathiya, A. S. Prakash, K. Ramesha, J. M. Tarascon and A. K. Shukla, *J. Am. Chem. Soc.*, 2011, **133**, 16291.
38 M. S. Whittingham, *Chem. Rev.*, 2004, **104**, 4271.
39 Y. Wei, C. W. Ryu and K. B. Kim, *J. Alloys Compd.*, 2008, **459**, L13.
40 X. Rui, J. Zhu, W. Liu, H. Tan, D. Sim, C. Xu, H. Zhang, J. Ma, H. H. Hng, T. M. Lim and Q. Yan, *RSC Adv.*, 2011, **1**, 117.
41 G. Du, K. H. Seng, Z. Guo, J. Liu, W. Li, D. Jia, C. Cook, Z. Liu and H. Liu, *RSC Adv.*, 2011, **1**, 690.
42 (*a*) T. Zhai, H. Liu, H. Li, X. Fang, M. Liao, L. Li, H. Zhou, Y. Koide, Y. Bando and D. Golberg, *Adv. Mater.*, 2010, **22**, 2547; (*b*) L. J. Fu, H. Liu, Y. P. Wu, E. Rahm, R. Holze and H. Q. Wu, *Prog. Mater. Sci.*, 2005, **50**, 881.
43 Z. Chen, Y. Qin, D. Weng, Q. Xiao, Y. Peng, X. Wang, H. Li, F. Wei and Y. Lu, *Adv. Funct. Mater.*, 2009, **19**, 3420.
44 W. Tang, X. Gao, Y. Zhu, Y. Yue, Y. Shi, Y. P. Wu and K. Zhu, *J. Mater. Chem.*, 2012, **22**, 20143.
45 (*a*) T. Sumura and M. Inagaki, *Solid State Ionics*, 1997, **104**, 183; (*b*) T. Brezesinski, J. Wang, S. H. Tolbert and B. Dunn, *Nat. Mater.*, 2010, **9**, 146.
46 H. Farsi, F. Gobal, H. Raissi and S. Moghiminia, *J. Solid State Electrochem.*, 2010, **14**, 643.
47 I. Shakir, M. Shahid, H. W. Yang and D. J. Kang, *Electrochim. Acta*, 2010, **56**, 376.
48 G. R. Li, Z. L. Wang, F. L. Zheng, Y. N. Ou and Y. X. Tong, *J. Mater. Chem.*, 2011, **21**, 4217.
49 (*a*) J. Hu, A. Ramadan, F. Luo, B. Qi, X. Deng and J. Chen, *J. Mater. Chem.*, 2011, **21**, 15009; (*b*) T. Tao, Q. Y. Chen, H. P. Hu and Y. Chen, *Mater. Lett.*, 2012, **66**, 102; (*c*) W. Tang,

 This journal is © The Royal Society of Chemistry 2013

Published on 16 avril 2013. Downloaded on 2024-08-15 14:15:36.

L. L. Liu, Y. S. Zhu, H. Sun, Y. P. Wu and K. Zhu, *Energy Environ. Sci.*, 2012, **5**, 6909.

50 (*a*) J. H. Park and O. O. Park, *J. Power Sources*, 2002, **111**, 185; (*b*) F. K. Cheng, C. He, D. Shu, H. Y. Chen, J. Zhang, S. Q. Tang and D. E. Finlow, *Mater. Chem. Phys.*, 2011, **131**, 268; (*c*) K. Kvastek and V. Horvat-Radosevic, *J. Electroanal. Chem.*, 2001, **511**, 65.

51 (*a*) J. J. Niu, W. G. Pell and B. E. Conway, *J. Power Sources*, 2006, **156**, 725; (*b*) Z. B. Wen, Q. T. Qu, Q. Gao, Z. H. Hu, Y. P. Wu, X. W. Zheng, Y. F. Liu and X. J. Wang, *Electrochem. Commun.*, 2009, **11**, 715; (*c*) C. W. Huang, C. T. Hsieh, P. L. Kuo and H. Teng, *J. Mater. Chem.*, 2012, **22**, 7314.

52 (*a*) S. W. Lee, B. S. Kim, S. Chen, Y. S. Horn and P. T. Hammond, *J. Am. Chem. Soc.*, 2009, **131**, 671; (*b*) K. Esumi, M. Ishigami, A. Nakajima, K. Sawada and H. Honda, *Carbon*, 1996, **34**, 279; (*c*) T. Ramanathan, F. T. Fisher, R. S. Ruoff and L. C. Brinson, *Chem. Mater.*, 2005, **17**, 1290; (*d*) Y. Y. Shao, J. Wang, M. Engelhard, C. M. Wan and Y. H. Lin, *J. Mater. Chem.*, 2010, **20**, 743.

53 (*a*) Y. T. Kim and T. Mitani, *J. Power Sources*, 2006, **158**, 1517; (*b*) D. N. Futaba, K. Hata, T. Yamada, T. Hiraoka, Y. Hayamizu, Y. Kakudate, O. Tanaike, H. Hatori, M. Yumura and S. Iijima, *Nat. Mater.*, 2006, **5**, 987.

54 (*a*) C. C. Hu, K. H. Chang, M. C. Lin and Y. T. Wu, *Nano Lett.*, 2006, **6**, 2690; (*b*) B. O. Park, C. D. Lokhande, H. S. Park, K. D. Jung and O. S. Joo, *J. Power Sources*, 2004, **134**, 148; (*c*) W. Sugimoto, T. Shibutani, Y. Murakami and Y. Takasu, *Electrochem. Solid-State Lett.*, 2002, **5**, A170; (*d*) C. C. Hu, H. Y. Guo, K. H. Chang and C. C. Huang, *Electrochem. Commun.*, 2009, **11**, 1631.

55 Y. Su, F. Wu, L. Bao and Z. Yang, *New Carbon Mater.*, 2007, **22**, 53.

56 H. Li, R. Wang and R. Cao, *Microporous Mesoporous Mater.*, 2008, **111**, 32.

57 P. C. Chen, G. Shen, Y. Shi, H. Chen and C. Zhou, *ACS Nano*, 2010, **4**, 4403.

58 (*a*) Y. T. Kim, K. Tadai and T. Mitani, *J. Mater. Chem.*, 2005, **15**, 4914; (*b*) J. S. Ye, H. F. Cui, X. Liu, T. M. Lim, W. D. Zhang and F. S. Sheu, *Small*, 2005, **1**, 560; (*c*) W. C. Fang, O. Chyan, C. L. Sun, C. T. Wu, C. P. Chen, K. H. Chen, L. C. Chen and J. H. Huang, *Electrochem. Commun.*, 2007, **9**, 239; (*d*) R. K. Das, B. Liu, J. R. Reynolds and A. G. Rinzler, *Nano Lett.*, 2009, **9**, 677.

59 (*a*) Z. S. Wu, D. W. Wang, W. Ren, J. Zhao, G. Zhou, F. Li and H. M. Cheng, *Adv. Funct. Mater.*, 2010, **20**, 3595; (*b*) Z. Algharaibeh, X. Liu and P. G. Pickup, *J. Power Sources*, 2009, **187**, 640.

60 (*a*) W. Wei, X. Cui, W. Chen and D. Ivey, *Chem. Soc. Rev.*, 2011, **40**, 1697; (*b*) M. S. Hong, S. H. Lee and S. W. Kim, *Electrochem. Solid-State Lett.*, 2002, **5**, A227; (*c*) V. Khomenko, E. R. Pinero and F. Béguin, *J. Power Sources*, 2006, **153**, 183.

61 (*a*) H. A. Mosqueda, O. Crosnier, L. Athouël, Y. Dandeville, Y. Scudeller, P. Guillemet, D. M. Schleich and T. Brousse, *Electrochim. Acta*, 2010, **55**, 7479; (*b*) S. Li, L. Qi, L. Lu and H. Wang, *RSC Adv.*, 2012, **2**, 6741.

62 (*a*) M. Xu, L. Kong, W. Zhou and H. Li, *J. Phys. Chem. C*, 2007, **111**, 19141; (*b*) H. Jiang, C. Z. Li, T. Sun and J. Ma, *Chem. Commun.*, 2012, **48**, 2606.

63 G. R. Li, Z. P. Feng, Y. N. Ou, D. C. Wu, R. W. Fu and Y. X. Tong, *Langmuir*, 2010, **26**, 2209.

64 A. Yuan and Q. Zhang, *Electrochem. Commun.*, 2006, **8**, 1173.

65 L. Bao, J. Zang and X. Li, *Nano Lett.*, 2011, **11**, 1215.

66 H. Zhang, G. P. Cao, Z. Y. Wang, Y. S. Yang, Z. J. Shi and Z. N. Gu, *Nano Lett.*, 2008, **8**, 2664.

67 K. S. Kim and S. J. Park, *J. Solid State Electrochem.*, 2012, **16**, 2751.

68 J. Yan, T. Wei, W. M. Qiao, Z. J. Fan, L. J. Zhang, T. Y. Li and Q. K. Zhao, *Electrochem. Commun.*, 2010, **12**, 1279.

69 Q. Cheng, J. Tan, J. Ma, H. Zhang, N. Shinya and L. C. Qin, *Carbon*, 2011, **49**, 2917.

70 Y. Hou, Y. Cheng, T. Hobson and J. Liu, *Nano Lett.*, 2010, **10**, 2727.

71 S. Dong, X. Chen, L. Gu, X. Zhou, L. Li, Z. Liu, P. Han, H. Xu, J. Yao, H. Wang, X. Zhang, C. Shang, G. Cui and L. Chen, *Energy Environ. Sci.*, 2011, **4**, 3502.

72 X. Lang, A. Hirata, T. Fujita and M. Chen, *Nat. Nanotechnol.*, 2011, **6**, 232.

73 M. Toupin, T. Brousse and D. Belanger, *Chem. Mater.*, 2004, **16**, 3184.

74 B. Djurfors, J. N. Broughton, M. J. Brett and D. G. Ivey, *J. Mater. Sci.*, 2003, **38**, 4817.

75 B. Djurfors, J. N. Broughton, M. J. Brett and D. G. Ivey, *Acta Mater.*, 2005, **53**, 957.

76 A. J. Roberts and R. C. T. Slade, *Electrochim. Acta*, 2010, **55**, 7460.

77 (*a*) Y. Cheng, S. Lu, H. Zhang, C. V. Varanasi and J. Liu, *Nano Lett.*, 2012, **12**, 4206; (*b*) A. Yuan, X. Wang, Y. Wang and J. Hu, *Energy Convers. Manage.*, 2010, **51**, 2588; (*c*) L. Demarconnay, E. R. Pinero and F. Béguin, *J. Power Sources*, 2011, **196**, 580; (*d*) L. Zhou, L. C. Yang, P. Yuan, J. Zou, Y. P. Wu and C. Z. Yu, *J. Phys. Chem. C*, 2010, **114**, 21868.

78 (*a*) R. N. Reddy and R. G. Reddy, *J. Power Sources*, 2006, **156**, 700; (*b*) I. Stojkovic, N. Cvjeticanin, I. Pašti, M. Mitric and S. Mentus, *Electrochem. Commun.*, 2009, **11**, 1512.

79 (*a*) D. Li and Y. Xia, *Nano Lett.*, 2003, **3**, 555; (*b*) G. Wee, H. Z. Soh, Y. L. Cheah, S. G. Mhaisalkar and M. Srinivasan, *J. Mater. Chem.*, 2010, **20**, 6720; (*c*) D. Sun, C. W. Kwon, G. Baure, E. Richman, J. Maclean, B. Dunn and S. H. Tolbert, *Adv. Funct. Mater.*, 2004, **14**, 1197; (*d*) L. M. Chen, Q. Y. Lai, Y. J. Hao, Y. Zhao and X. Y. Ji, *J. Alloys Compd.*, 2009, **467**, 465.

80 (*a*) L. Yu, C. X. Zhao, X. Long and W. Chen, *Microporous Mesoporous Mater.*, 2009, **126**, 58; (*b*) W. C. Fang, *J. Phys. Chem. C*, 2008, **112**, 11552; (*c*) M. Jayalakshmi, M. M. Rao, N. Venugopal and K. B. Kim, *J. Power Sources*, 2007, **166**, 578; (*d*) Y. Yang, D. Kim, M. Yang and P. Schmuki, *Chem. Commun.*, 2011, **47**, 7746.

81 (*a*) L. T. Lam and R. Louey, *J. Power Sources*, 2006, **158**, 1140; (*b*) P. K. Shen and X. L. Wei, *Electrochim. Acta*, 2003, **48**, 1743.

82 (*a*) N. Yu, L. Gao, S. Zhao and Z. Wang, *Electrochim. Acta*, 2009, **54**, 3835; (*b*) P. N. Bartlett, T. Dunford and M. A. Ghanem, *J. Mater. Chem.*, 2002, **12**, 3130; (*c*) L. X. Ding, F. L. Zheng, J. W. Wang, G. R. Li, Z. L. Wang and Y. X. Tong, *Chem. Commun.*, 2012, **48**, 1275.

83 (*a*) S. G. Kandalkar, D. S. Dhawale, C. K. Kim and C. D. Lokhande, *Synth. Met.*, 2010, **160**, 1299; (*b*) R. Tummala, R. K. Guduru and P. S. Mohanty, *J. Power*

Published on 16 avril 2013. Downloaded on 2024-08-15 14:15:36.

Sources, 2012, **209**, 44; (*c*) L. Y. Gong, X. H. Liu, L. H. Su and L. Q. Wang, *J. Solid State Electrochem.*, 2012, **16**, 297.
84 (*a*) Z. Fan, J. H. Chen, K. Z. Cui, F. Sun, Y. Xu and Y. F. Kuang, *Electrochim. Acta*, 2007, **52**, 2959; (*b*) J. Yan, T. Wei, W. M. Qiao, B. Shao, Q. K. Zhao, L. J. Zhang and Z. J. Fan, *Electrochim. Acta*, 2010, **55**, 6973; (*c*) X. W. Wang, S. Q. Liu, H. Y. Wang, F. Y. Tu, D. Fang and Y. H. Li, *J. Solid State Electrochem.*, 2012, **16**, 3593.
85 (*a*) C. C. Hu, J. C. Chen and K. H. Chang, *J. Power Sources*, 2013, **221**, 128; (*b*) X. B. Ji, P. M. Hallam, S. M. Houssein, R. Kadara, L. M. Lang and C. E. Banks, *RSC Adv.*, 2012, **2**, 1508; (*c*) J. M. Ko, D. Soundarajan, J. H. Park, S. D. Yang, S. W. Kim, K. M. Kim and K. H. Yu, *Curr. Appl. Phys.*, 2012, **12**, 341.
86 (*a*) U. Kohler, C. Antonius and P. Bauerlein, *J. Power Sources*, 2004, **127**, 45; (*b*) J. W. Lang, L. B. Kong, M. Liu, Y. C. Luo and L. Kang, *J. Solid State Electrochem.*, 2010, **14**, 1533; (*c*) J. H. Park, S. W. Kim, O. O. Park and J. M. Ko, *Appl. Phys. A: Mater. Sci. Process.*, 2006, **82**, 593; (*d*) J. H. Zhong, A. L. Wang, G. R. Li, J. W. Wang, Y. N. Ou and Y. X. Tong, *J. Mater. Chem.*, 2012, **22**, 5656.
87 (*a*) G. P. Wang, L. Zhang, J. Kim and J. J. Zhang, *J. Power Sources*, 2012, **217**, 554; (*b*) J. H. Park, O. O. Park, K. H. Shin, C. S. Jin and J. H. Kim, *Electrochem. Solid-State Lett.*, 2002, **5**, H7.
88 J. H. Park, S. W. Kim, O. Park and J. M. Ko, *Appl. Phys. A: Mater. Sci. Process.*, 2006, **82**, 593.
89 R. R. Salunkhe, K. Jang, S. W. Lee and H. Ahn, *RSC Adv.*, 2012, **2**, 3190.
90 (*a*) Y. G. Wang, L. Yu and Y. Y. Xia, *J. Electrochem. Soc.*, 2006, **153**, A743; (*b*) H. Wang, H. S. Casalongue, Y. Liang and H. Dai, *J. Am. Chem. Soc.*, 2010, **132**, 7472; (*c*) S. Nohara, T. Asahina, H. Wada, N. Furukawa, H. Inoue, N. Sugoh, H. Iwasaki and C. Iwakura, *J. Power Sources*, 2006, **157**, 605.
91 (*a*) Y. G. Wang, J. Y. Luo, C. X. Wang and Y. Y. Xia, *J. Electrochem. Soc.*, 2006, **153**, A1425; (*b*) W. Tang, L. L. Liu, S. Tian, L. Li, Y. B. Yue, Y. P. Wu, S. Y. Guan and K. Zhu, *Electrochem. Commun.*, 2010, **12**, 1524.
92 G. J. Wang, Q. T. Qu, B. Wang, Y. Shi, S. Tian, Y. P. Wu and R. Holze, *Electrochim. Acta*, 2009, **54**, 1199.
93 G. J. Wang, L. J. Fu, N. H. Zhao, L. C. Yang, Y. P. Wu and H. Q. Wu, *Angew. Chem., Int. Ed.*, 2007, **46**, 295.
94 (*a*) G. J. Wang, L. C. Yang, Q. T. Qu, B. Wang, Y. P. Wu and R. Holze, *J. Solid State Electrochem.*, 2010, **14**, 865; (*b*) M. Winter, J. O. Besenhard, M. E. Spahr and P. Novák, *Adv. Mater.*, 1998, **10**, 725.
95 Y. P. Wu, X. Y. Yuan, C. Dong and J. Y. Duan, *Lithium Ion Batteries: Practice and Applications* (2nd Edi.), Chemical Industry Press, Beijing, 2012.
96 (*a*) K. M. Shaju and P. G. Bruce, *Chem. Mater.*, 2008, **20**, 5557; (*b*) F. Jiao, J. L. Bao, A. H. Hill and P. G. Bruce, *Angew. Chem., Int. Ed.*, 2008, **47**, 9711.
97 (*a*) W. Li, J. R. Dahn and D. Wainwright, *Science*, 1994, **264**, 1115; (*b*) W. Li and J. R. Dahn, *J. Electrochem. Soc.*, 1995, **142**, 1472.
98 M. J. Zhang and J. R. Dahn, *J. Electrochem. Soc.*, 1996, **143**, 2730.
99 M. Zhao, X. Song, F. Wang, W. Dai and X. Lu, *Electrochim. Acta*, 2011, **56**, 5673.
100 I. B. Stojkovic, N. D. Cvjeticanin and S. V. Mentus, *Electrochem. Commun.*, 2010, **12**, 371.
101 A. Yuan, L. Tian, W. Xu and Y. Wang, *J. Power Sources*, 2010, **195**, 5032.
102 W. Xu, A. Yuan and Y. Wang, *J. Solid State Electrochem.*, 2012, **16**, 429.
103 F. X. Wang, S. Y. Xiao, Y. Shi, L. L. Liu, Y. S. Zhu, Y. P. Wu, J. Z. Wang and R. Holze, *Electrochim. Acta*, 2013, **93**, 301.
104 G. J. Wang, Q. T. Qu, B. Wang, Y. Shi, S. Tian and Y. P. Wu, *ChemPhysChem*, 2008, **9**, 2299.
105 (*a*) L. Tian and A. Yuan, *J. Power Sources*, 2009, **192**, 693; (*b*) N. Cvjeticanin, I. Stojkovic, M. Mitric and S. Mentus, *J. Power Sources*, 2007, **174**, 1117; (*c*) G. J. Wang, H. P. Zhang, L. J. Fu, B. Wang and Y. P. Wu, *Electrochem. Commun.*, 2007, **9**, 1873.
106 L. Liu, F. Tian, X. Wang, Z. Yang, Q. Chen and X. Wang, *J. Solid State Electrochem.*, 2012, **16**, 491.
107 Y. G. Wang, J. Y. Lou, W. Wu, C. X. Wang and Y. Y. Xia, *J. Electrochem. Soc.*, 2007, **154**, A228.
108 G. J. Wang, L. J. Fu, B. Wang, N. H. Zhao, Y. P. Wu and R. Holze, *J. Appl. Electrochem.*, 2008, **38**, 579.
109 J. Zheng, J. J. Chen, X. Jia, J. Song, C. Wang, M. S. Zheng and Q. F. Dong, *J. Electrochem. Soc.*, 2010, **157**, A702.
110 R. B. Shivashankaraiah, H. Manjunatha, K. C. Mahesh, G. S. Suresh and T. V. Venkatesha, *J. Solid State Electrochem.*, 2012, **16**, 1279.
111 (*a*) X. Pétrissans, A. Bétard, D. Giaume, P. Barboux, B. Dunn, L. Sicard and J. Y. Piquemal, *Electrochim. Acta*, 2012, **66**, 306; (*b*) A. Mirmohseni, M. S. S. Dorraji and M. G. Hosseini, *Electrochim. Acta*, 2012, **70**, 182; (*c*) C. Xu, B. Li, H. Du and F. Kang, *Angew. Chem., Int. Ed.*, 2012, **51**, 933.
112 (*a*) J. Jiang, Y. Li, J. Liu, X. Huang, C. Yuan and X. W. Lou, *Adv. Mater.*, 2012, **24**, 5166; (*b*) W. Li, F. Zhang, Y. Dou, Z. Wu, H. Liu, X. Qian, D. Gu, Y. Xia, B. Tu and D. Zhao, *Adv. Energy Mater.*, 2011, **1**, 382; (*c*) W. Zhou, L. Lin, W. Wang, L. Zhang, Q. Wu, J. Li and L. Guo, *J. Phys. Chem. C*, 2011, **115**, 7126; (*d*) Y. Luo, J. Luo, J. Jiang, W. Zhou, H. Yang, X. Qi, H. Zhang, H. J. Fan, D. Y. W. Yu, C. M. Li and T. Yu, *Energy Environ. Sci.*, 2012, **5**, 6559; (*e*) P. L. Taberna, S. Mitra, P. Poizot, P. Simon and J. M. Tarascon, *Nat. Mater.*, 2006, **5**, 567; (*f*) J. Jiang, J. P. Liu, W. W. Zhou, J. H. Zhu, X. T. Huang, X. Y. Qi, H. Zhang and T. Yu, *Energy Environ. Sci.*, 2011, **4**, 5000.
113 (*a*) D. H. Jurcakova, A. M. Puziy, O. I. Poddubnaya, F. S. García, J. M. D. Tascon and G. Q. Lu, *J. Am. Chem. Soc.*, 2009, **131**, 5026; (*b*) W. Yang, T. P. Fellinger and M. Antonietti, *J. Am. Chem. Soc.*, 2011, **133**, 206.
114 (*a*) A. I. Najafabadi, D. N. Futaba, S. Iijima and K. Hata, *J. Am. Chem. Soc.*, 2010, **132**, 18017; (*b*) K. S. Kang, Y. S. Meng, J. Breger, C. P. Grey and G. Ceder, *Science*, 2006, **311**, 9.
115 J. N. Tiwari, R. N. Tiwari and K. S. Kim, *Prog. Mater. Sci.*, 2012, **57**, 724.

 This journal is © The Royal Society of Chemistry 2013